

# Chapter 1

## Analysis

In the following chapter the various parts of the measurements done for this thesis are explained. The following chapter contains seven sections explain each of these parts: mc simulation, trigger development, data sets and event selection, break-up determination, signal extraction, efficiency determination, and systematic checks. In Section 1.1 the simulations used to estimated the detectors ability to measure UPC processes is discussed. Section 1.2 explains the considerations that went into the triggers which were developed for the analyses discussed in this thesis. How the final events were selected and how triggers were used to separate the data in to data sets is detailed in Section 1.3. Extraction of the number of events from each of the three physics processes discussed in this thesis, coherent, incoherent, and photon-photon process from the final selected events is discussed in Section 1.5. The estimates of the detectors efficiency for measuring UPC events is explained in Section 1.6. Section ?? lays out how the systematic uncertainties are estimated.

### 1.1 MC Simulation

Every physical measurement is the product of the underlying physics convolved with the response of the detector used to do the measurement. In order to understand the underlying physical process, the detector's effect on the measurement must be understood and accounted for. As instruments become more and more complicated, the interplay between all of the many parts of the detector

19 makes an analytic approach to the problem untenable. For this reason, the numerical technique of  
20 Monte Carlo (MC) simulation is the most useful approach.

21 MC simulations use random number generation to solve the problem numerically by brute  
22 force. First, particles are generated according the theoretical distributions. These particles are  
23 then propagated through a simulation of the detector. As the particles pass through the detector,  
24 random numbers are again used to determine how these particles interact with the materials of the  
25 detector based on the known properties of the material. In this way, the theoretical distributions  
26 are merged with the complicated response of the detector. The collective combination of the many  
27 sub detectors responses with the theoretical distributions emerges from the successive creation of  
28 random events. The result is the convolved response of the detector with the underlying physical  
29 process that is to be studied.

30 In this thesis, two main classes of MC simulation samples were used. The first class uses  
31 STARlight to generate events. This class of MC samples corresponds to the theoretical calculations  
32 described in in Section ???. There are three different physical process described. Coherent  $J/\psi$   
33 production, where the photon couples to the nucleus as a whole, incoherent  $J/\psi$  production, where  
34 the photon couples to a nucleon within the nucleus, and photon-photon process, where the photons  
35 from the two nuclei interact with each other to produce a lepton pair directly. All three STARlight  
36 sample produce a  $\mu^+$  and  $\mu^-$  in the final state that interacts with the detector. The second class  
37 uses PYTHIA6 to decay  $J/\psi$  with a given input  $p_T$  and rapidity distribution. Two samples of  
38 this class of particle gun data were produced each with different  $p_T$  distributions (See Fig.).

39 The software chain used for producing the STARlight samples has five steps. Because STARlight  
40 is not integrated into the standard CMS software framework (CMSSW), this chain was developed  
41 for the analysis described in this thesis. First, STARlight is run in the specified mode, and a sin-  
42 gle file is created for each physics process, for this thesis, one file for the coherent process, the  
43 incoherent process, and the photon-photon process for a total of three files. The output from the  
44 STARlight generator is in a format specific to STARlight, therefore, the output from the original  
45 generation step is then converted to the Les Houches (LHE) format. In this conversion to LHE

format, either the parent  $J/\psi$  for the  $J/\psi$  production samples, or the initial photon-photon pair are added to the LHE output file. The standard STARlight output only includes the final state particles. Additionally, the initial output from STARlight is split into a collection of smaller LHE files so that each of the smaller samples can be processed in parallel. Each of the LHE files is used as input to CMSSW. The three remaining steps take place within the framework. First the generated particles are propagated through the GEANT4 detector simulation. This accounts for all the interactions with the detector and produces as output a format identical to the raw data that is recorded during data taking. The next two steps are identical to data taking. The reconstruction software used during data taking is run on the output of the detector simulation, and last, the output of the reconstruction is reduced to the information that is needed for the final analysis.

The particle gun samples were created entirely within CMSSW. An interface to PYTHIA6 is included within CMSSW, which takes  $J/\psi$   $p_T$  and rapidity distributions as input. The  $J/\psi$  are created according to the input distributions, and then uses PYTHIA6 to decay the  $J/\psi$ s to  $\mu^+$  and  $\mu^-$ . As with the STARlight samples, these muons are propagated through the GEANT4 simulation of the detector, and the raw data is produced. The remaining steps of running the reconstruction code and reducing the data to the final data needed for the analysis are identical to the STARlight production.

The five MC samples, three STARlight samples, and two particle gun samples, differ primarily in the  $p_T$  distribution of the  $J/\psi$ s produced and the polarization of the  $J/\psi$ s, which effects angle at which the muon daughters are emitted relative to the direction in which the  $J/\psi$  is traveling. In Fig. 1.1 the  $p_T$  of  $J/\psi$ s from the coherent and photon-photon samples are peaked steeply at a low  $p_T$ , and neither sample extends much beyond 0.15 GeV in  $p_T$ . The incoherent sample is peaked near 0.5 GeV and extends beyond 1 GeV. The two particle gun samples resemble the incoherent and coherent samples. The first sample has a Gaussian  $p_T$  distribution extending to approximately 0.15 GeV, whereas the second is flat in  $p_T$  up to 2 GeV. The particle gun samples are unpolarized, whereas the STARlight samples have transverse polarization. Therefore, the particle gun samples there is no preferred direction for the emission of the daughter muons. In the STARlight samples

73 however the daughters tend to be emitted in line with the direction of the  $J/\psi$ 's momentum. This  
 74 is particularly pronounced for the photon-photon process.

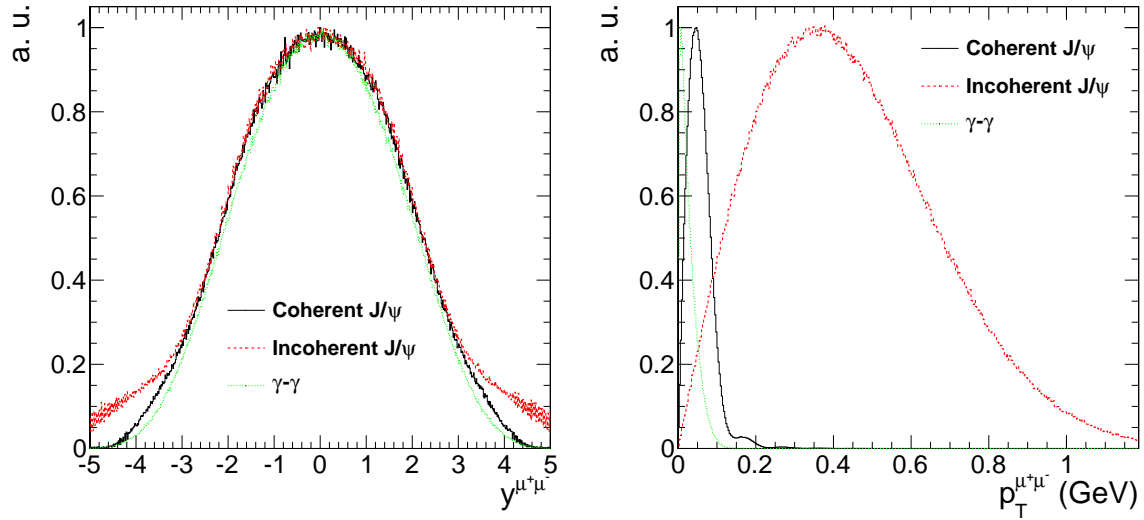


Figure 1.1: Generator level rapidity (left) and  $p_T$  (right) distributions for the coherent, **incoherent**, and **photon-photon** process

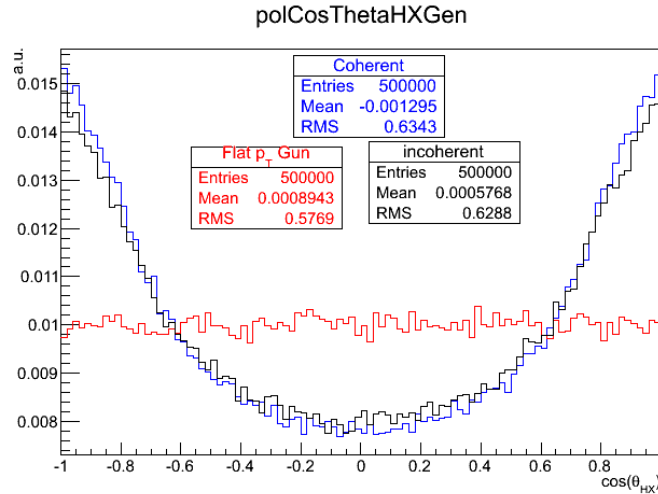


Figure 1.2: The  $J/\psi$  polarization of the **particle gun**, **coherent**, and incoherent samples are plotted as the cosine of the helicity angle.

75 The momentum of the final state muons is the main drivers of whether the candidate can be  
 76 measured. The polarization and the  $p_T$  distribution of dimuons from the generator determine the  
 77 momentum of the daughters. The low  $p_T$  of the  $J/\psi$  restricts the momentum of the  $\mu^+$  and  $\mu^-$

daughters produced from the  $J/\psi$  decay. The polarization effects how the momentum is shared between the daughters. In the rest frame of the parent particle from which the daughters decay equal momentum is given to each daughter. However in the lab frame of the detector, the muon daughters which are emitted from transversely polarized  $J/\psi$  will tend to be emitted in the direction of  $J/\psi$  and will have unequal momentum in the lab frame. The daughter traveling in the direction of the  $J/\psi$  will have increased momentum, whereas the daughter traveling opposite to the  $J/\psi$  direction will have decreased momentum. The combination of these two effects create a muon with very low momentum compared to the typical momenta of muons measured by CMS. The momentum of the lower momentum muon daughters is the main restriction on whether or not the  $J/\psi$  can be measured.

## 1.2 Trigger Development

Prior to the 2011 LHC PbPb run, UPC events had not been directly studied in PbPb collisions using CMS. Design of the UPC triggers required studies of the 2010 data to estimate rates and insure that the bandwidth used by these trigger would be sufficiently low. All the different physics analyses must share the limited readout rate of the detector. For this reason, conservation of bandwidth was a major design consideration.

To estimate the 2011 rates prior to the run, the 2010 rates were used to extrapolate to the interaction rate of the 2011 run. The unique UPC triggers were estimated by combining existing triggers from the 2010 run. By calculating the ratio between the UPC trigger rates and the minimum bias trigger rate, the UPC trigger rates were scaled up to the 2011 interaction rates using the 2010 data. The extrapolated rates allowed for a package triggers to be created that fit within the bandwidth requirement of CMS Heavy Ions group.

The trigger package for 2011 contained ZDC based efficiency monitoring triggers, muon and electron based triggers for measuring  $J/\psi$ , and backup triggers in case there was a problem with the original muon and electron triggers. In order to recorded the trigger efficiency monitoring

data, the ZDC triggers had to be prescaled to a lower rate. The scaling down of the monitoring triggers were setup to insure overlap with the signal triggers. By balancing the competing objectives of rate reduction and increasing the overlap between the monitoring and signal triggers, the prescales for the trigger were as seen in Table .

### 1.2.1 L1 Trigger

The goal of the L1 triggers was to record enough data to measure dimuons and dielectrons in UPC events. To achieve this, the loosest muon trigger and lowest threshold ECAL triggers were paired with a trigger on energy in the ZDC and a veto on energy in the BSC. Additional triggers which vetoed on energy in HF were commissioned in case radiation damaged to the BSCs. The L1 package that was constructed for the analysis of UPC  $J/\psi$  is presented in Table 1.1.

L1 Trigger Seed	Type
L1_MuOpen_ZdcCalo_NotBscMinBiasThresh2_BptxAND	Physics
L1_EG2_ZdcCalo_NotBscMinBiasThresh2_BptxAND	Physics
L1_EG5_ZdcCalo_NotBscMinBiasThresh2_BptxAND	Physics
L1_ZdcCaloMinus_BptxAND	Monitor
L1_ZdcCaloMinus_BptxAND	Monitor
L1_MuOpen_ZdcCalo_NotHcalHfCoincidencePm_BptxAND	Backup
L1_EG2_ZdcCalo_NotHcalHfCoincidencePm_BptxAND	Backup
L1_EG5_ZdcCalo_NotHcalHfCoincidencePm_BptxAND	Backup

Table 1.1: List of 2011 L1 seeds.

The cumulative L1 trigger rate for all the UPC L1 trigger seeds was required to be 200 Hz. This requirement stemmed from the need to keep the tracker read-out rate low. The trackers baseline voltage can fluctuate due to the high tracker hit multiplicities in PbPb collisions. In order to monitor the zero suppression of the tracker, the zero suppression algorithm was executed using the HLT computing farm rather than the in the tracker firmware. The rate at which the tracker could be readout without zero suppression set the limit for the L1 bandwidth.

## 1.2.2 HLT Trigger

As opposed to the L1 trigger, which reads out the tracker, the HLT has access to the tracker information. Reconstruction of a track in the pixel detector is used by the UPC paths. The use of the pixel detector only, as opposed to using the whole tracker including the silicon strip detector, allows for quick track reconstruction saving computing cycles. The requirement of at least one reconstructed pixel track for the HLT triggers was designed to reject backgrounds where no particles are reconstructed by the tracker.

HLT Trigger	
HLT_HIUPCNeuMuPixel_SingleTrack	Physics
HLT_HIUPCNeuEG2Pixel_SingleTrack	Physics
HLT_HIUPCNeuEG5Pixel_SingleTrack	Physics
HLT_HIMinBiasZDC_Calo_PlusOrMinus_v1	Monitor
HLT_HIMinBiasZDC_PlusOrMinusPixel_SingleTrack_v1	Monitor
HLT_HIUPCNeuHcalHfMuPixel_SingleTrack	Backup
HLT_HIUPCNeuHcalHfEG2Pixel_SingleTrack	Backup
HLT_HIUPCNeuHcalHfEG5Pixel_SingleTrack	Backup

Table 1.2: List of 2011 HLT trigger.

The total HLT output for the UPC trigger package was 20 Hz. The limiting factor for the HLT rate was the amount of disk space available to store the data. To meet the bandwidth the requirements and collected a significant sample of data for estimating efficiencies, the prescales for the triggers were set. The ZDC trigger that was passed through from the L1 was given a larger prescale to account for the higher rate relative to the more selective ZDC path, which also required a pixel track on the HLT.

## 1.3 Data Sets and Event Selection

In order to investigate novel physics processes like UPC  $J/\psi$  production, the LHC has delivered unprecedented amounts of data. The data for this analysis was recorded during the 2011 LHC PbPb run. During this period,  $150 \mu b^{-1}$  were recorded by the CMS detector, corresponding to

over a billion PbPb collisions. Of this,  $143 \mu b^{-1}$  are used in this analysis.

### 1.3.1 Data Set

Three specially selected samples were used for the present analysis (see Table 1.3). These samples were recorded using subsets of the triggers found in Section 1.2. The  $J/\psi$  events discussed in this thesis were obtained analyzing the sample labeled in Table 1.3 as physics. A ZDC triggered sample was recorded for the sake of estimating efficiencies. Last, a zero bias sample was recorded for investigating the ZDC and the noise distributions of HF. By recording this hierarchy of samples, interesting events are selected with a much higher purity in the physics sample, while the zero bias and ZDC triggered samples allow for the investigation of the selection criteria.

To record the physics sample containing the  $J/\psi$  signal, a muon trigger was paired with a veto on energy in the BSC and a requirement that there be energy in at least one of two sides of the ZDC. This trigger utilizes the unlikely chance of having overlapping noise in in the ZDC and muon detector. Because of the characteristically low momentum of UPC  $J/\psi$  as compared to  $J/\psi$  created by other physics process, the loosest muon trigger was used. By pairing the muon trigger with the ZDC on the L1, the noise contribution was reduced from the noise contribution from either of the two sub-detectors to the noise coincidence between the two sub-detectors. Contributions from hadronic interactions are reduced by the veto on the BSC. In this way the balance between reducing the rate and maximizing the efficiency was struck, allowing for the data to be recorded without producing high rates resulting in dead time for the detector.

In order to investigate the muon trigger and the other parts of the event selection, a minimum bias sample was recorded using the ZDC. For ZDC triggered sample, any event which had energy consistent with at least one neutron in either of the two sides of the ZDC was recorded. This process is much more common than the UPC  $J/\psi$  production. For this reason, the rates of this trigger are much higher than the physics trigger, and only a small sub set of these events are recorded. From this trigger the pixel track portion of the HLT trigger efficiency was estimated.

In addition to the minimum bias and physics sample, a zero bias sample was recorded to ex-



Sample	Events	$L_{int}$
Physics	300K	143.3 $\mu b$
Minimum Bias	100K	X
Zero Bias	5M	580 b

Table 1.3: Integrated luminosities and number of events for the three samples used in this analysis.

amine the ZDC trigger and the HF noise distributions. The zero bias trigger fired every time both beams passed through CMS. Only 4 events out of every million triggered were recorded for this sample. This sample allowed for an unbiased measurement of the ZDC trigger efficiency as discussed in Section 1.6. Because the zero bias trigger does not require any activity in any of the CMS sub detectors, the sample contains very few hadronic collisions. This allowed for a measurement of the electronic noise distributions in the HF, which will be discussed in the next section.

The integrated luminosity for each of the three samples is calculated by recording activity in HF [?]. The cross section for HF activity is measured from a van der Meer scan, and the cross section was found to be X. In this way the amount of integrated luminosity for any running period is related to the activity in HF. An additional method was used to cross check the integrated luminosity obtained by the van der Meer scan technique. The integrated luminosity can also be measured by counting the events that fire the L1 minimum bias trigger together with the inelastic PbPb cross section.

### 1.3.2 Event selection

The analysis described in this thesis focuses on UPC  $J/\psi$  decaying to muons. The trigger used for this analysis recored 346841 events. A set of off-line cuts were applied to increase the relative contribution of UPC events to background processes. The following cuts were applied.

Two sets of event selection cuts were applied to reject background events. The first set rejects background from the beam. The second rejects events where hadronic collisions have occurred.

To reject beam induced background the following cuts were applied:

- The reconstructed vertex must be within X cm in the transverse direction and X cm in the

cut	cut type	events
all triggered	–	346841
good vertex requirement	beam background rejection	340997
beam halo muon rejection	beam background rejection	302777
cluster shape compatibility requirement	beam background rejection	233590
single-sided neutron requirement	hadronic interaction rejection	149992
two track requirement	hadronic interaction rejection	32732
HF signal rejection	hadronic interaction rejection	5392
muon quality requirement	fake muon rejection	1956
$J/\psi$ mass requirement	kinematic cut	662
muon detectability cuts	kinematic cut	541

Table 1.4: Effects of event selection cuts.

longitudinal direction. This cut insures that reconstructed particles come from interactions between the two beams rather than event where one of the two beams interact with gas particles near the interaction point.

- Beam halo muons were rejected using the timing of the muon hits. The beam halo cut rejects events where muons surrounding the beam stream through the detector.
- Pixel cluster shape should be compatible with the vertex. This cut requires that energy deposits in the silicon tracker point back to the reconstructed primary vertex.

These beam background cuts do not reject any UPC  $J/\psi$  candidates.

The second set of background rejection cuts were designed to reduce contamination from hadronic interactions.

- No more than 2 reconstructed tracks in the event. The track requirement rejects events that produce many charged particles.
- Maximum reconstructed hit energy in HF was required to be below the threshold for electronic noise. Nearly all hadronic interactions ( $\sim 98\%$ ) produce particles in the range  $3 < |\eta| < 5$  covered by the HF detector. By requiring that the energy deposits in HF resemble noise, nearly all elastic hadronic collisions are expected to be rejected.

- Energy in the ZDCs consistent with neutrons on only one side of the interaction point. In hadronic interactions both nuclei break-up. By requiring that ZDC only reconstruct neutrons on one side of the interaction point, hadronic interactions that produce neutrons on both sides were rejected.

Each of these cuts are designed to reject topologies produced by hadronic interactions. The effect of these cuts can be seen in Table X.

To establish the HF noise thresholds, the noise distributions were measured in zero bias events. Only presences of both beams was required for these events to be recorded. An Off-line selection of events with no reconstructed tracks was used to insure that no collision had taken place. The HF noise threshold was defined as the cut that keeps %99 of the zero bias events. The noise distribution from this zero bias sample is compared to the physics sample and MC in Fig. 1.3.

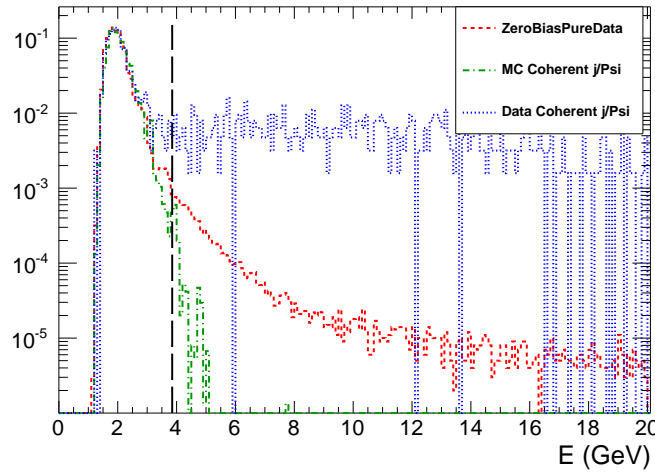


Figure 1.3: Comparison of HF noise distributions in zero bias data, physics triggered data, and MC.

The following standard muon quality cuts are applied:

- Tracker track matched with at least one muon segment (in any station) in both X and Y coordinates ( $< 3 \sigma$ ).
- Cut on number of tracker layers with hits  $> 5$ .

- Number of pixel layers  $> 0$ .
- The  $\chi^2$  per degrees of freedom of the track fit  $< 3$ .
- Loose transverse and longitudinal impact parameter cuts, with in 3 cm in the transverse direction and withing 30 cm in the longitudinal direction with respect to the primary vertex.

These cuts are applied to reduce the number of fake muons.

## 1.4 Break up determination

As described in Section: ??, UPC  $J/\psi$  photoproduction can be accompanied by the emission of neutrons from either of the two colliding nuclei. The various neutron emission scenarios, or break-up ~~break-up~~ modes, can be distinguished by the ZDC. By separating events where the ZDC signal is consistent with 1 neutron versus several neutrons, the different break-up modes can be separated and compared to theory. For this reason, reconstruction of the ZDC signal plays an important role in this thesis. In order to maximize the ability to explore the one neutron peak, which sits at the bottom of the ZDCs dynamic range, a new ZDC reconstruction method was devised. This new reconstruction method was ~~than~~then used to establish a one neutron and many neutron threshold. In this section the ZDC signal reconstruction is described and how the neutron thresholds on this signal were set.

### 1.4.1 ZDC ~~Signal-Reconstruction~~signal reconstruction

The ZDC signal is built up from the pulse shapes for each of the 18 individual ZDC channels. The pulse shape is recorded in 250 ns second chunks and is divided into 10 time slices of 25 ns (See Fig 1.4). Counting from 0, the 4th time slice is synced with the timing of the rest of the detector and corresponds to when the products of the recorded collision reached the ZDC. For this reason the channel signal is taken from the 4th time slice.

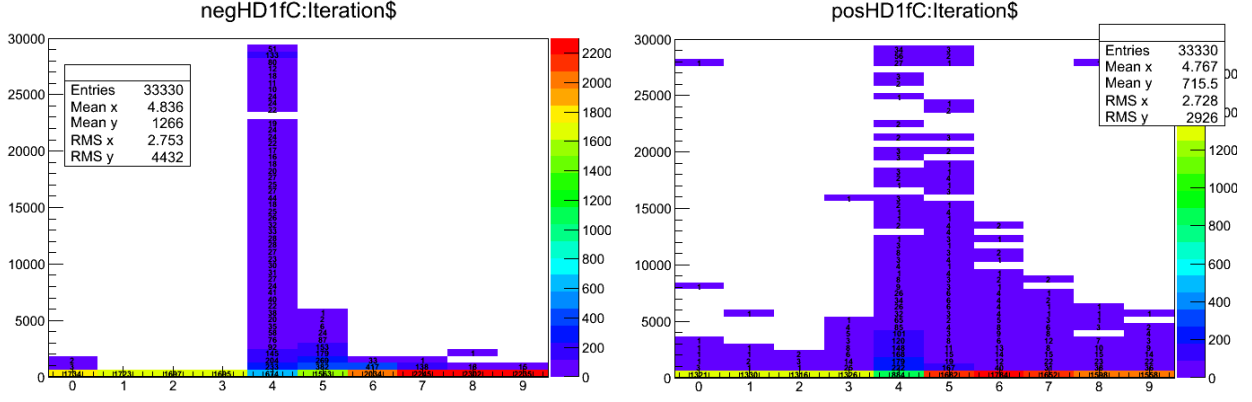


Figure 1.4: Average ZDC pluse shape is plotted as the charge as a function of time slice for the first hadronic from ZDC<sup>-</sup> (left) and ZDC<sup>+</sup> (right).

The ZDC signal sits on top of a low frequency noise pedestal. Over the time scale of 250 ns, this low frequency noise signal appears as a constant that shifts randomly from event to event. The contribution from this noise is therefore measured event by event in order to subtract it. Time slice 5 is used for this purpose.

Time slices 1 and 2 could also be used to estimate the low frequency noise. However because the noise fluctuates to negative values of charge that ~~can't be measured by the QIE~~ cannot be measured, these time ~~slice~~ slices can only provide a measurement of the noise half the time. By using time slice 5 which contains the falling tail of the signal, the noise can be measured any time the signal raises significantly above the noise. If the fraction of signal in time slice 4 and 5 are constant and the noise contributes the same value to both time slices, the following formula is applicable:

$$Ts4 \propto (Ts4 + C) - (Ts5 + C) = Ts4 - R_{Ts5/Ts4} * Ts4 = Ts4(1 - R_{Ts5/Ts4}), \quad (1.1)$$

where  $Ts4$  is the signal contribution in time slice 4,  $Ts5$  is the signal contribution to time slice 5,  $C$  is a random noise constant from the low frequency noise, and  $R_{Ts5/Ts4}$  is the ratio between the signal contribution from time slice 5 over time slice 4. Fig. 1.5 demonstrates the consistence of the fraction and validates the unconventional method of using the falling tail of the signal to estimate

the low frequency noise. By using time slice 5 ~~the chances~~, the chances of measuring the noise are maximized ~~allowing for the possibility to operate the~~. Separating the signal from the noise ~~and~~ measure ~~is especially important because~~ the ZDC signal ~~near~~ for the one neutron peak sits near the noise at the bottom of the ZDC dynamic range.

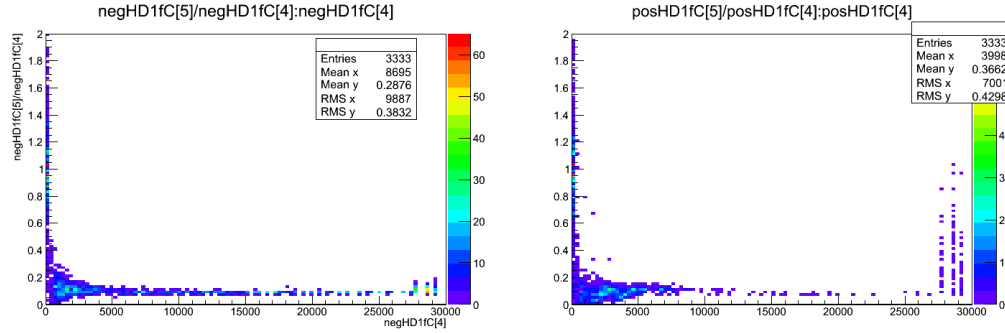


Figure 1.5: The fraction of signal in time slice 5 over time slice 4 as a function of the signal in time slice 5 in  $ZDC^-$  (left) and  $ZDC^+$  (right).

To measure one signal value for  $ZDC^+$  and one for  $ZDC^-$ , the signals from each of the channels are combined. Channels from the EM section and HD section are combined first. Only channels with signal above zero in time slice 5 and time slice 4 are included. The EM section of the calorimeter is more densely packed with optical fibers and therefore has a higher gain relative to the HAD section. To account for this, the combination of EM channels is weighted with a factor of 0.1 to match the HAD channel gains. The value for each side of the ZDC's signal is given by the sum of the HAD channel combination and weighted EM channel combination. It is this signal, one for  $ZDC^+$  and one for  $ZDC^-$ , which is plotted in Fig. 1.6 to measure the neutron thresholds.

## 1.4.2 Determination of the one neutron thresholds

The ZDC thresholds used to establish the various break-up modes were measured from zero bias data. By using this dataset, the neutron spectrum does not contain a trigger bias. ~~The trigger requirement for the zero bias events is~~ Zero bias trigger required that both beams were present in CMS. This does ~~however~~, however, include a significant electronic noise contribution due to events where no neutrons are emitted in the direction of the ZDC.

To determine the thresholds for one and multiple neutrons, the  $ZDC^+$  and  $ZDC^-$  spectra are were fit. Four Gaussian functions were combined to fit the spectra. The electronic noise was fit to a Gaussian about around zero. The one, two, and three neutron peaks are fit to Gaussians that are successively broader. The mean of each peak was initially set to multiples of the mean of the one neutron peak. The threshold for a neutron in the ZDC was taken from the fits in Fig. 1.6.

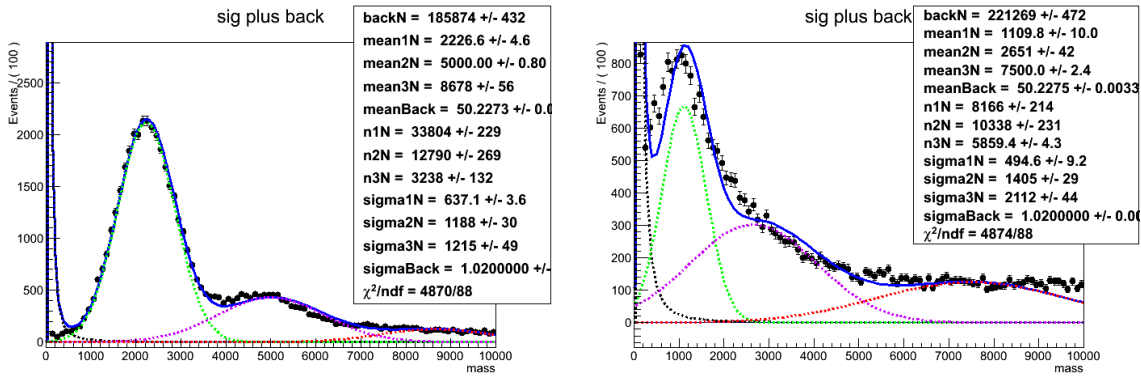


Figure 1.6: Fit to the signal spectra for  $ZDC^-$  (left) and  $ZDC^+$  (right)

Any signal greater  $2\sigma$  below the mean of the one neutron peak was considered signal. Any signal greater than  $2\sigma$  above was considered multiple neutrons. In this way the single neutron break up modes could be separated from the multiple neutron modes.

Several of the break-up mode calculations that have been done involve single sided configurations where neutrons are present on one side of the interaction point and not the other. To identify signal consistent with noise, noise distributions for the combined EM sections and the combined HAD sections were measured. The beams are only made to collide every 200 ns. In Fig. 1.4 higher than average signal can be seen in the 0th time slice, which precedes the main signal time slice time slice 4 by 200 ns. This is due to events where activity was present in the ZDC for two consecutive collisions. Time slices 1 and 2, however, occurred between collisions. These time slices were used to estimate the noise spectrum.

Fig 1.7 shows the noise spectrum for each of the EM and HAD sections for the two sides of the ZDC. As with the signal measurements, the low frequency noise pedestal is subtracted event by event by subtracting time slice 2 from time slice one before the channel signals are combined

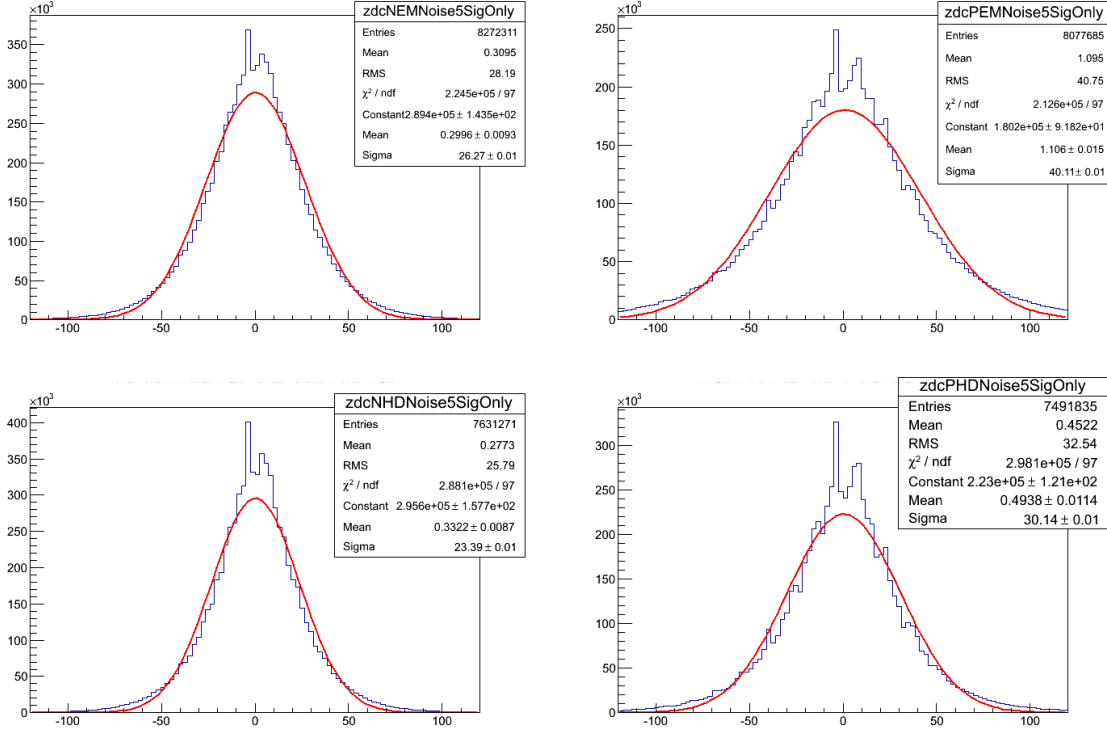


Figure 1.7: ZDC noise spectra from ZDC<sup>-</sup> EM section (upper left), ZDC<sup>+</sup> EM section (upper right), ZDC<sup>-</sup> HAD section (lower left), and ZDC<sup>+</sup> HAD section (lower right).

for each section. A side is considered consistent with noise if both HAD section and EM section signal measurements from the signal method involving time slice 4 and time slice 5 are lower than 2 sigma below the mean in Fig. 1.7. With the single ~~neutron~~neutron, multi-neutron, and noise thresholds established, the contributions to the various break-up modes were estimated and compared to theory.

## 1.5 Signal extraction

After all event selection cuts, the coherent  $J/\psi$ , incoherent  $J/\psi$ , and photon-photon process all contribute to the remaining events. Each process must be separated from the final mix. To achieve this, the invariant mass and  $p_T$  distributions are used to distinguish between the three processes. The photon-photon process is extended in invariant mass whereas the  $J/\psi$  is peak strongly near 3.1 GeV. In  $p_T$  the photon-photon and coherent process have similar distributions, both peaked shapely



below 0.1 GeV, whereas the incoherent process is more broadly distributed across an interval extending to nearly 1 GeV. The mass distribution was ~~fitted~~fit to separate the photon-photon process from the  $J/\psi$  process. The  $p_T$  distribution was used to separate the incoherent process from the photon-photon process, and the coherent process. In this way, a separate yield was extracted for all three processes.

The invariant mass distribution for opposite sign dimuons is shown in Fig. 1.8. A  $J/\psi$  signal is clearly visible together with tails at higher and ~~in~~ lower mass due to the photon-photon process. A fit to the invariant mass distribution was done using a Gaussian to account for the  $J/\psi$  signal and a first order polynomial function for the photon-photon process. The extracted number of  $J/\psi$  candidates from this fit includes all  $J/\psi$ s in the mass window that passed the analysis cuts, i.e. both coherent and incoherent process contribute to yield from the mass fit. The  $p_T$  distribution is needed to separate the two different contributions to the  $J/\psi$  peak.

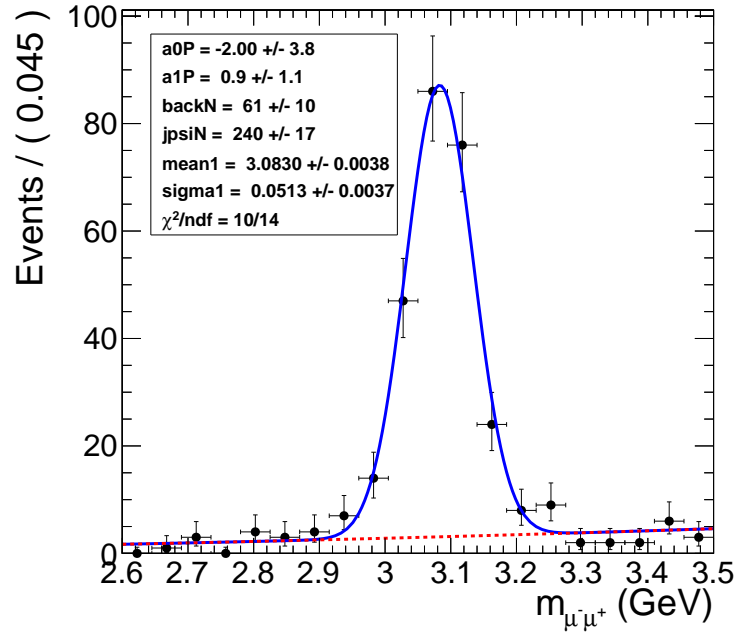


Figure 1.8: Mass fit to  $J/\psi$  using Gaussian for the signal and a first order polynomial for the photon-photon continuum

The same candidates from Fig. 1.8 ~~are~~were plotted as a function of  $p_T$  in Fig. 1.9. The clear overlap of the coherent and photon-photon process, and the clear separation of these two lower

313  $p_T$  processes from the incoherent process ~~are~~ is apparent. The shape of the  $p_T$  distribution for  
 314 the coherent, incoherent, and photon-photon process are taken from the final output of MC after  
 315 applying all analysis cuts. To obtain the yields for each of the three process, the  $p_T$  distribution  
 316 was fit to the three templates. In Fig.1.9, the yield parameters that were fit were left unconstrained  
 317 for all three process.

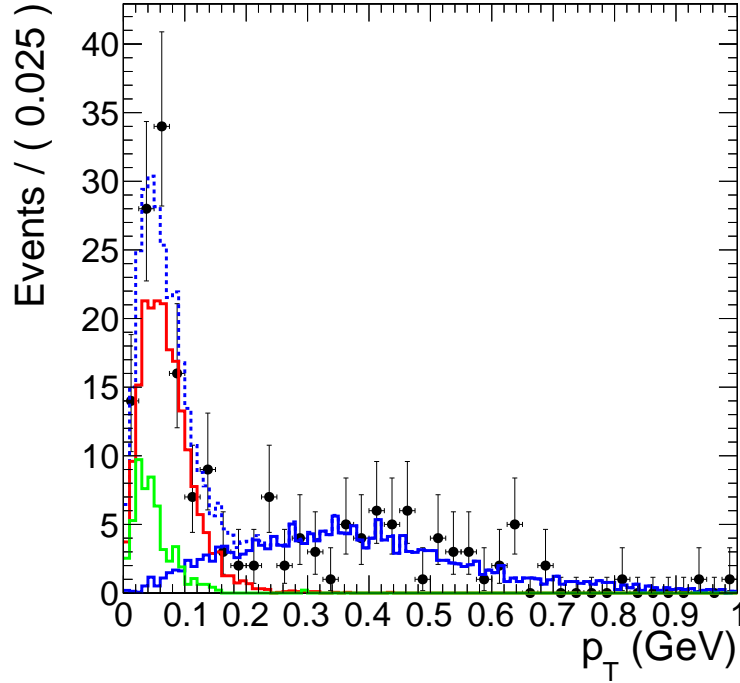


Figure 1.9: Fit to MC  $p_T$  templates.

318 The shape of the photon-photon ~~process~~ and coherent  $J/\psi$  process are very similar in  $p_T$ . Ac-  
 319 cordingly, the contribution from the photon-photon process and the coherent process are difficult  
 320 to separate from the  $p_T$  distribution. The confidence contours in Fig. 1.10 from the template fit  
 321 in Fig. 1.9 demonstrate the strong anti-correlation between the coherent yield parameter,  $nCo$ , and  
 322 the yield parameter for the photon-photon process,  $nGamma$ . Because of the anti-correlation, the  
 323 statistical uncertainty on  $nCo$  and  $nGamma$  from the fit are larger than  $\sqrt{nCo}$  and  $\sqrt{nGamma}$  ex-  
 324 pected from Poisson statistics. The information from the invariant mass and  $p_T$  distributions ~~was~~  
 325 were combined to break this correlation. Through this combination, the contribution to the final  
 326 yield from the three process was measured.

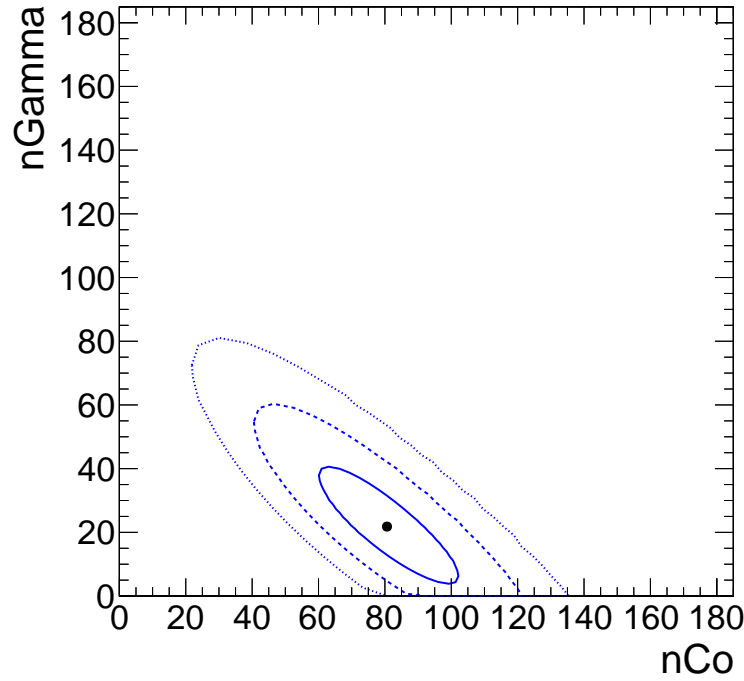


Figure 1.10: 68%, 95%, and 99% confidence contours from the  $p_T$  template fit.

To utilize the mass fits ability to distinguish the photon-photon process from the coherent and incoherent process all while utilizing the  $p_T$  fits ability to separate the coherent and photon-photon processes from the incoherent, a simultaneous fit to the mass spectrum and  $p_T$  spectrum was pre-formed. Fig. 1.11 shows the result of the simultaneous fit. The simultaneous fit forces the parameter  $nGamma$  to both describe the photon-photon continuum present in the side bands of the  $J/\psi$  mass peak as well the photon-photon contribution to the low- $p_T$  part of the  $p_T$  spectrum. In addition, the  $J/\psi$  yield from the mass fit is forced to equal the contribution from the incoherent and coherent process in the fit to the  $p_T$  distribution. In this way, the correlation between the yield parameters was broken, and the contribution from the three process are left were made independent of each other.

By simultaneously fitting both the mass and  $p_T$  spectra, the yields from the coherent, incoherent, and photon-photon process were separated from each other in total yield of final candidates. The ambiguity between the coherent and incoherent processes in the mass fit and the ambiguity between the coherent and the photon-photon process was over come by combining the two fits through used

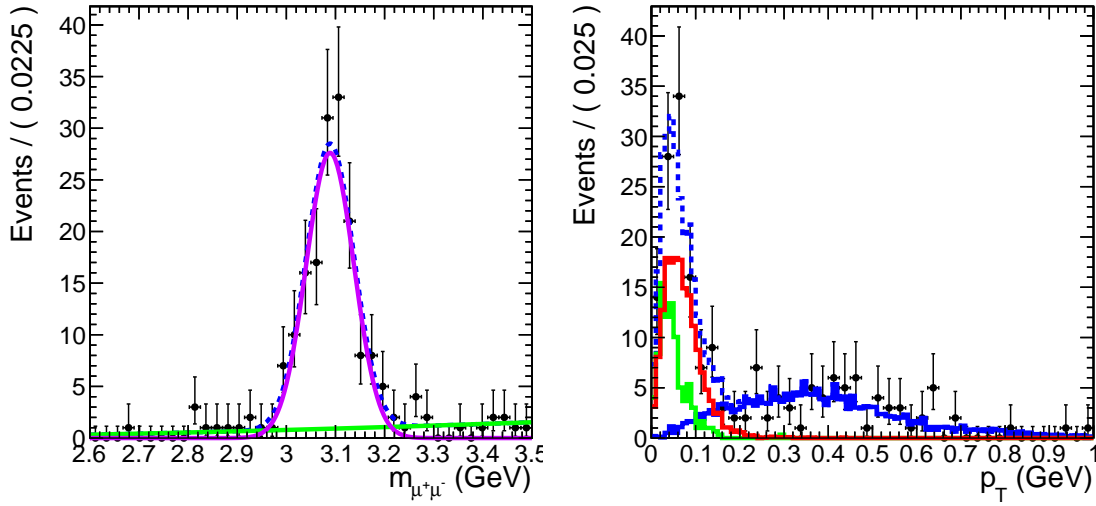


Figure 1.11: Simultaneous fit to the mass and  $p_T$  spectra.

of the simultaneous fit. Fig. 1.12 shows the confidence contours for  $nCo$  and  $nGamma$  from the simultaneous fit in Fig. 1.11. The slope of the confidence contours in Fig. 1.12 is noticeably closer to 0 than the apparent negative slope in Fig. 1.10. The contours for the simultaneous fit are also reduced compared to Fig. 1.10 with widths in  $nCo$  and  $nGamma$  similar to those expected from Poisson statistics. From the simultaneous fit, reasonable statistical errors were obtained along with the yields for the three processes.

## 1.6 Efficiency determination

### 1.6.1 Muon Efficiencies

The muon efficiencies are measured from MC and data. The MC based measurement accounts for the detector acceptance and the efficiency of the muon quality discussed in Section 1.3. The trigger efficiencies were measured in data using the tag and probe method [?], which is discussed below.

CMS has a limited acceptance for  $J/\psi$ , particularly in the case of  $J/\psi$  with low momentum like those produced in UPC events. To measure the acceptance of CMS for  $J/\psi$ , reconstructed dimuon candidates were considered detectable if both reconstructed daughters fell

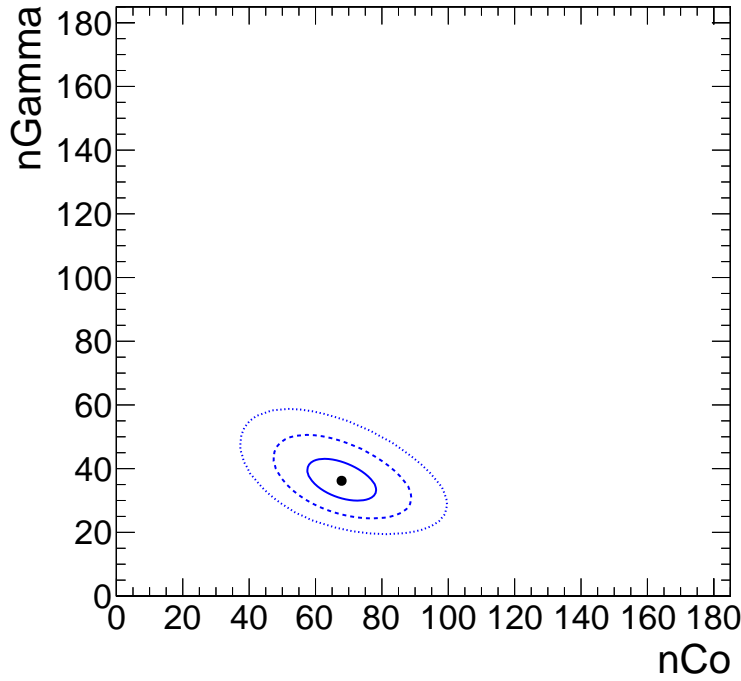


Figure 1.12: 68%, 95%, and 99% confidence contours from the simultaneous fit.

into a detectability region. This region was defined using the coherent  $J/\psi$  events obtained from STARlight. The efficiency for reconstructing single muons  $\epsilon_{reco}^\mu$  is defined by  $\epsilon_{reco}^\mu = \frac{N_{reco}^\mu}{N_{gen}^\mu}$ , where  $N_{reco}^\mu$  is the number reconstructed muons ~~after after~~ obtained after the full CMS detector simulation and that ~~pass-passed~~ passed the standard muon quality cuts, and  $N_{gen}^\mu$  is the number of generated muons from STARlight. Fig. 1.13 shows the efficiency for reconstructing single muons from coherent  $J/\psi$  events. To avoid the edges of the detectors acceptance, all reconstructed muons that fall into a  $(p_T, |\eta|)$  bin that has an efficiency less than 20% were rejected thus defining the detectability region. The acceptance for reconstructing dimuons was calculated from MC using the following formula:

$$A = \frac{N_{det}(|y|, p_T)}{N_{gen}(|y|, p_T)}, \quad (1.2)$$

where  $N_{det}$  is the number of reconstructed dimuons where both daughters fall ~~in-to~~ into the detectability region, and  $N_{gen}$  is the number of generated dimuons. From Eq. 1.2, the acceptance for  ~~$J/\psi$~~   $J/\psi$  was calculated as a function of  $|y|$ , and  $p_T$  (see Fig. 1.14).

The tag and probe method is used to measure the trigger efficiency of the muon daughters,

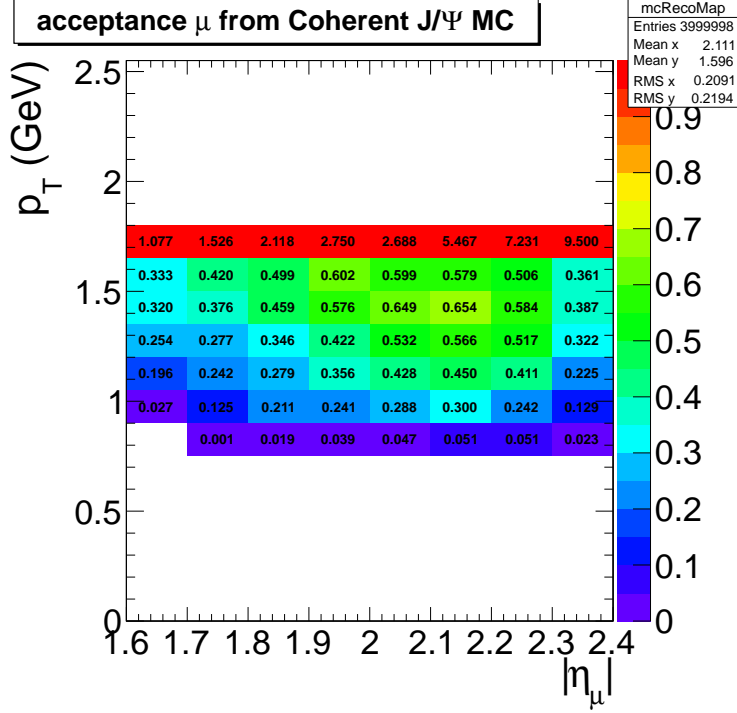


Figure 1.13: Muon daughter detectability from coherent  $J/\psi$ , incoherent  $J/\psi$ , photon-photon, and  $J/\psi$ -gun samples.

which is a data driven approach. In this method there are three categories of daughter muons. **Tag muons** are high quality muons. **Passing probes** are reconstructed muons that match the muon trigger, while **failing probes** do not. Each dimuon will have one daughter classified as a tag and the other as a probe. From here three invariant mass histograms are studied. One histogram is created from all pairs. The second comes from pairs where the probe is a passing probe. The last histogram comes from pairs where the probe fails to fulfill the trigger, *i.e.* the probe is a failing probe. Because this depends on the  $p_T$  and  $|\eta|$  of the probe, one set of three histograms for each  $(p_T, |\eta|)$  bin of the probe is created.

To extract the single muon trigger efficiency  $\epsilon_{trig}^\mu$ , each set of invariant mass histograms was simultaneously fitted. The signal was fitted using a Crystal Ball function, and the background was fitted to an exponential. The Crystal Ball parameters were simultaneously fitted to all three histograms. The exponential function was fitted to the failing and passing probe histograms separately. Because the background shapes are in **principal-principle** different for the two samples, the

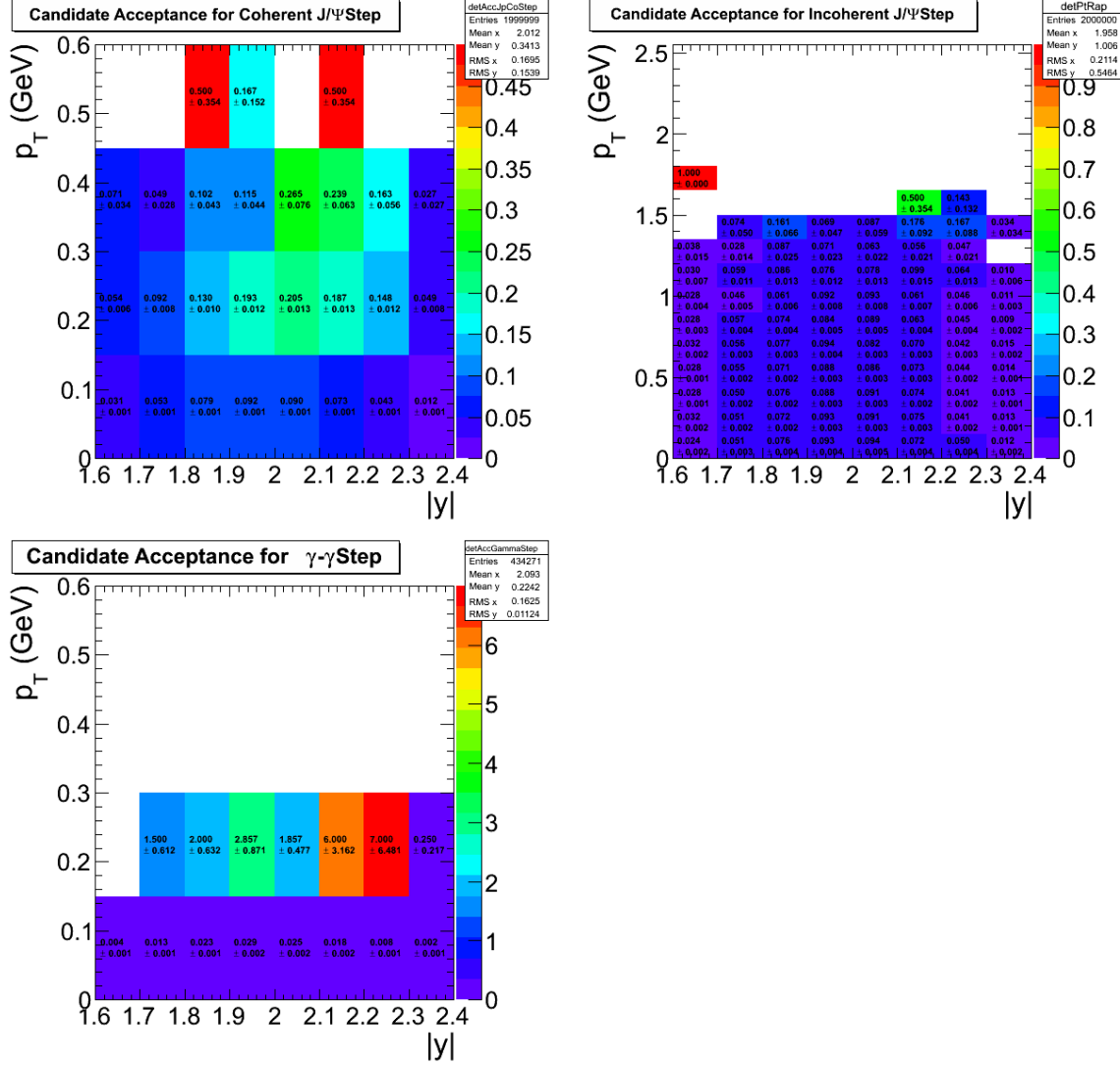


Figure 1.14: Dimuon acceptance from coherent  $J/\psi$  (top left), incoherent  $J/\psi$  (top right), and photon-photon interactions (lower).

efficiency is driven by this difference.

To measure the trigger efficiency a tag is required to pass all muon quality cuts and matched to the trigger. The probe is required to pass all quality cuts. A passing probe is a probe that is also matched to the trigger. In this way, the tag leaves the probe ~~in-biased~~unbiased by the trigger and the efficiency can be ~~measured by fitting mass~~measured by fitting the mass distribution.

Fig. 1.15 shows the fit of the three sets of pairs. This fit is done for each bin of the probes  $p_T$  and  $\eta$ . The resulting fit is in Fig. 1.16.

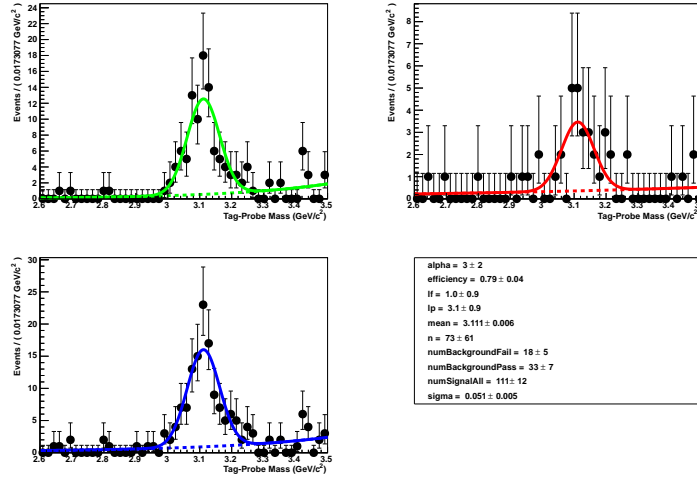


Figure 1.15: Fits to tag and probe pairs in the  $J/\psi$  mass region.

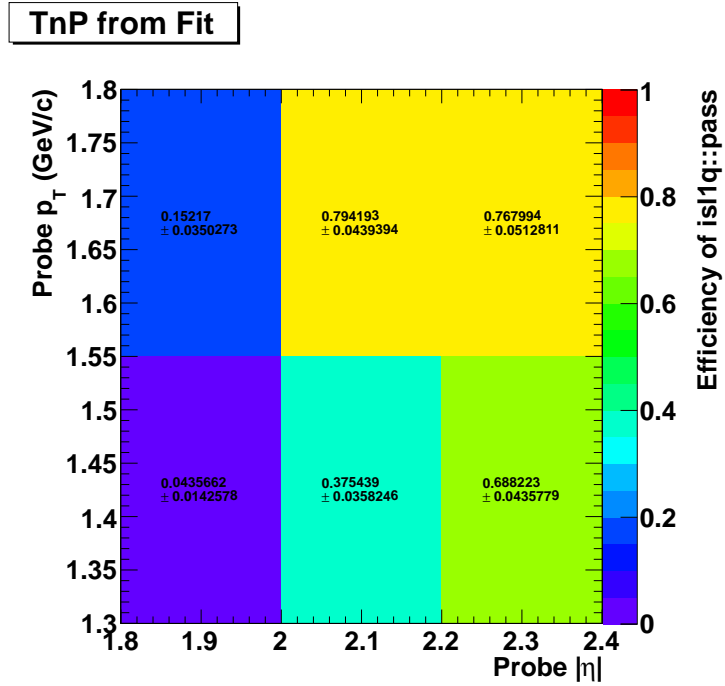


Figure 1.16: Muon trigger efficiencies in  $p_T$  and  $\eta$  bins from the tag and probe method.

388 The dimuon trigger efficiency  $\epsilon_{\text{dimuontrigger}}^{\text{dimuon}}$  was measured from the single muon effi-  
 389 ciencies. The efficiency of each candidate was calculated using the following equation:

$$\epsilon_{\text{dimuontrigger}}^{\text{dimuon}} = 1 - (1 - \epsilon_{\text{trigger}}^{\mu_1})(1 - \epsilon_{\text{trigger}}^{\mu_2}), \quad (1.3)$$



where  $\varepsilon_{trigger}^{\mu_1}$  is the tag and probe efficiency of the first dimuon daughter, and  $\varepsilon_{trigger}^{\mu_2}$  is the efficiency of the second muon daughter. In Eq. 1.3 the probability of at least one daughter firing the trigger is calculated by subtracting one from the probability that neither daughter fires the trigger, thus giving the dimuon trigger efficiency.

The average dimuon trigger efficiency for each dimuon  $(p_T, |y|)$  bin was calculated by averaging the individual dimuon candidates in each bin. The average trigger efficiency was multiplied

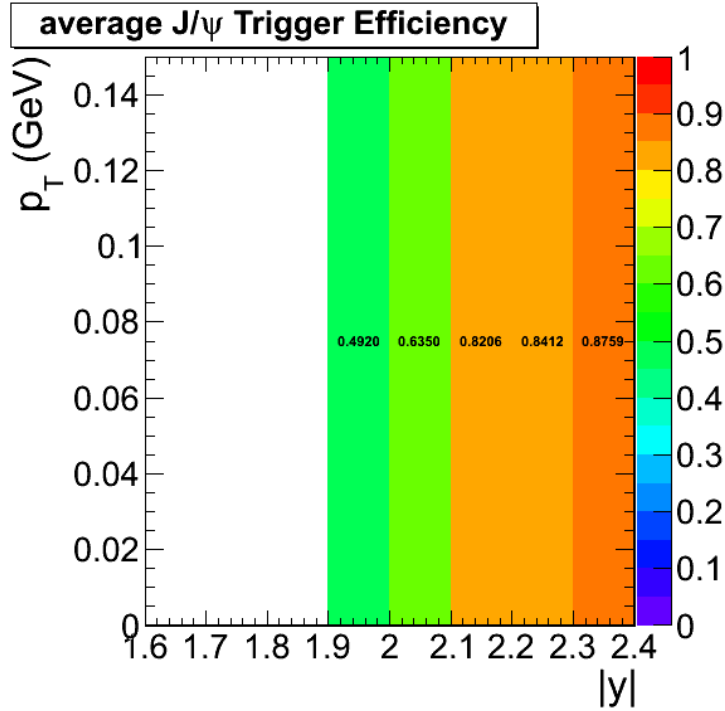


Figure 1.17: The trigger efficiency from tag and probe averaged over candidates in each  $(p_T, |y|)$  bin.

by the acceptance from the MC to produce a total ~~efficiency times acceptance factor~~ factor for both efficiency and acceptance.

The total combined efficiency and acceptance factor coherent  $J/\psi$  between  $2.0 < |y| < 2.2$  was found to be around 5%. The roughly 7% acceptance factor from the MC is the main contributor to the total efficiency. Primarily, the interplay of the polarization of the  $J/\psi$  and the material in detector drive down the efficiency by creating an effective momentum threshold for detection (see Section 1.1). The reconstruction efficiency of the daughters is ranges between 20%-60% for

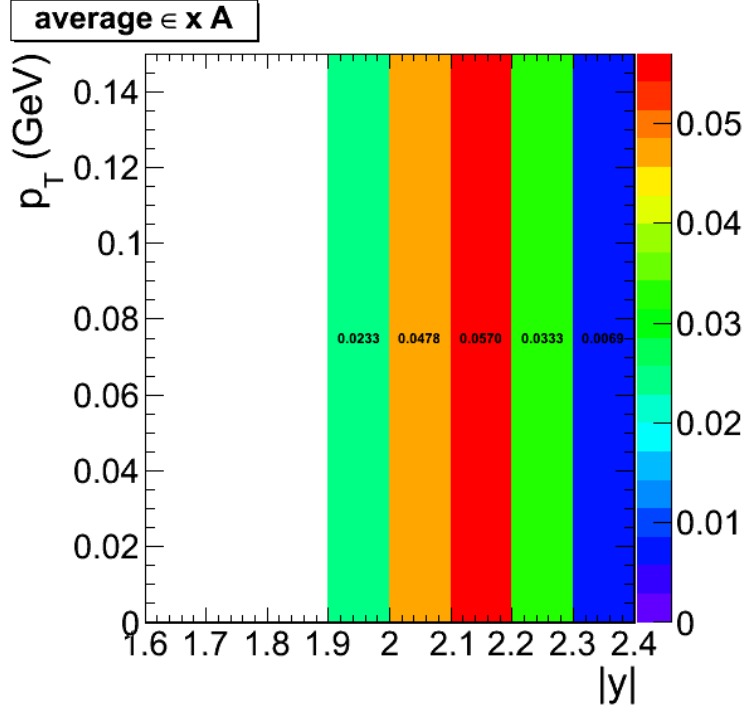


Figure 1.18: The acceptance times averaged trigger efficiency from tag and probe.

muons in the defined detectability range. The trigger efficiency for the detectable muons ranges from 30%-80% depending on  $p_T$ . The typical trigger efficiency for the dimuons was ranges from 60% to 80%.

## 1.6.2 ZDC trigger efficiency

As discussed in Section 1.4, a special trigger was prepared to monitor the ZDC trigger efficiency. This trigger required either a  $ZDC^+$  or  $ZDC^-$  trigger, together with at least one pixel track. Events were accepted offline if there was no activity in the BSCs or activity on a single side.

This sample suffers from a trigger bias. For example, a sample triggered by  $ZDC^+$  would always produce a  $ZDC^+$  trigger efficiency of one. To avoid this, the special trigger sample was divided into two subsamples in the following way. A first sample triggered by the  $ZDC^+$  input and second one triggered by the  $ZDC^-$ . The  $ZDC^+$  trigger efficiency is measured from the  $ZDC^-$  sample, and vice versa.

The trigger efficiency for reconstructed ZDC energies above the single neutron threshold were

ZDC Side	Reco Method	$N_{events}$	$N_{trig}$	$\epsilon_{ZDC}$
ZDC <sup>+</sup>	1	72946	71688	$0.982 \pm 0.005$
ZDC <sup>+</sup>	2	73028	71706	$0.9819 \pm 0.005$
ZDC <sup>-</sup>	1	76137	71786	$0.9429 \pm 0.005$
ZDC <sup>-</sup>	2	76132	71859	$0.9439 \pm 0.005$

Table 1.5: ZDC trigger efficiencies for ZDC reconstruction method 1 and 2

estimated (see for Sec. 1.4). The ZDC<sup>+</sup> efficiency was calculated using the ZDC<sup>-</sup> triggered sample. To estimate the efficiency, the number of events with energy in ZDC<sup>+</sup> greater than the single neutron threshold,  $N_{events}$ , were measured. From this set of events, the number of events that also fire the ZDC<sup>+</sup> ~~are~~was measured. The ratio between the number of single neutron events that ~~fire~~fired the trigger and all single neutron events was taken as the estimate of trigger efficiency. The same procedure ~~is~~was applied for each side of the ZDC. The trigger efficiency of the ZDC was found to be 98% for ZDC<sup>-</sup> and 94% for ZDC<sup>+</sup>.

## 1.7 Systematic checks

Table ?? shows the systematic errors that were estimated. The method used to separate the coherent from the photon-photon process is the most dominant error. The ZDC reconstruction method used to estimate the neutron thresholds is the next most dominant, followed by the method used to estimate the HF noise threshold.

systematic	uncertainty in %
Template fit normalized	+9.5% -12%
ZDC reconstruction	2.9%
ZDC trigger efficiency	2.2%
HF noise threshold	+1.3% -3.4%
MC acceptance	1.1%
<del>Mass fits 1.9%</del> Total systematic	8.1%

Table 1.6: Summary of systematic uncertainties

### 1.7.1 HF noise threshold

The way in which the HF noise distribution is measured effects the event selection and therefore the final candidate yeild. This cut plays a significant role in rejecting hadronic events. In Table 1.4 the importance of cutting on HF noise is evident. The HF noise cut rejects a little less than 1/5 of the remaining events. The systematic uncertainties on the HF noise requirement is important for this reason. The result must not depend significantly on the method used to apply the cut on the noise because of the large reduction of events that result from it.

Four different approaches were employed to estimate the systematic effect arising from picking a particular method for setting the HF noise threshold. By looking at the variation of the number of events that remain after applying the thresholds derived from these four methods, the systematic uncertainty for the HF noise cut was estimated. The four methods are derive from combinations of two variations. The type of object was varied from a low-level detector object called a RecHit to a higher level physics object called a CaloTower. The RecHit is the energy deposited in a single calorimeter detector element, where as the CaloTower is a collection of RecHits with varrious thresholds, which represent a full energy deposit that would come from a particle or a collection of particles from a jet passing through the detector. The second variation is on the separation of the two sides. In one case the threshold is derived for the two sides combined. In another case the thresholds are calculated separately for the two sides of HF. By combining these two variations, a total of four estimates of the effect of the HF noise cut were made. Table ?? below shows the thresholds that are measured for each of the four methods. The resulting yields from the four different methods are displayed in Table ??.

Object type	HF (GeV)	HF <sup>-</sup> (GeV)	HF <sup>+</sup> (GeV)
RecHits	3.85	3.25	3.45
CaloTowers	4.25	3.25	3.75

Table 1.7: HF noise theresholds for various noise measurement methods.

The threshold was adjusted to estimate the effect of tightening the requirement on the zero bias data. By successively lowering the percentage of the zero bias sample that was included, the HF

Object type	Combinded HF threshold	Two-sided thresholds
RecHits	298	290
CaloTowers	302	288

Table 1.8: Candidate yields below 1.05 GeV  $p_T$  for various HF noise cuts.

noise cut was made more restrictive including first 98%, than 97% of all zero bias events. This was done for both object types, RecHits and CaloTowers. This allows for an estimate of the systematic uncertainty on selecting a 99% cut. Table ?? shows the effect on the thresholds themselves for both RecHits and CaloTowers, whereas Table ?? shows the effect on the candidate yields.

Table 1.9: Values of the energy cuts for the HF calorimeter for RecHit and CaloTower in GeV.

%	$E_{RecHit}$ GeV	$E_{CaloTower}$ GeV
99	3.85	4.25
98	3.25	3.75
97	2.95	3.25

Table 1.10: Number of dimuon candidates with  $p_T < 1.05$  when changing HF calorimeter cuts for RecHit and CaloTower.

%	RecHit cut	CaloTower cut
99	298	302
98	287	294
97	284	280

The systematic uncertainty in the HF noise threshold measurement was calculated taking the difference from the 99% combined RecHit method with the upper and lower extrema. The systematic uncertainty from this method is calculated to be +1.3% -3.4%.

## 1.7.2 Template fit normalization

The  $p_T$  template fit depends on the functions chosen for the fit to the mass distribution. As described in Section 1.5, the similarity of the  $p_T$  distribution for the coherent and photon-photon process make the contributions from the two process difficult to separate from the  $p_T$

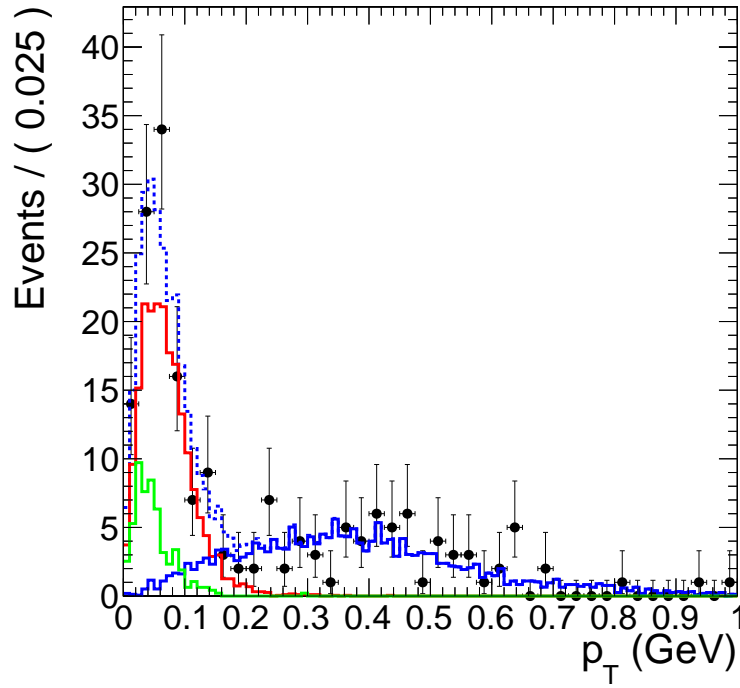


Figure 1.19: Coherent, incoherent, and photon-photon process  $p_T$  template fit to data.

distribution alone. The mass distribution was used to distinguish between these two processes. In turn, the  $p_T$  becomes dependent on the mass fit.

The systematic uncertainty due to the choose of functions used to fit the mass distribution was estimated by varying the signal and background functions. The contribution to the background from the mass fit was used to fix the contribution from the photon-photon process in the  $p_T$  template fit. Two functions were used to describe the signal, a Gaussian, and a Crystal ball function. The background was fit to a linear function, a 2nd order polynomial, and a 2nd order Cheby-Chev polynomial. The resulting variation on the coherent contribution was used to as an estimate of this systematic effect.

Moving from left to right in Fig ??, the contribution from the photon process increases. The  $\chi^2$  pre degree of freedom is similar between the three fits indicating a similar goodness of fit. On this basis, neither fit is preferred. The left most fit uses a Crystal Ball function to account for the radiative decay of the final state daughters of the  $J/\psi$ . The low mass exponential portion however picks up background events and overestimates the  $J/\psi$  contribution. The right most plot

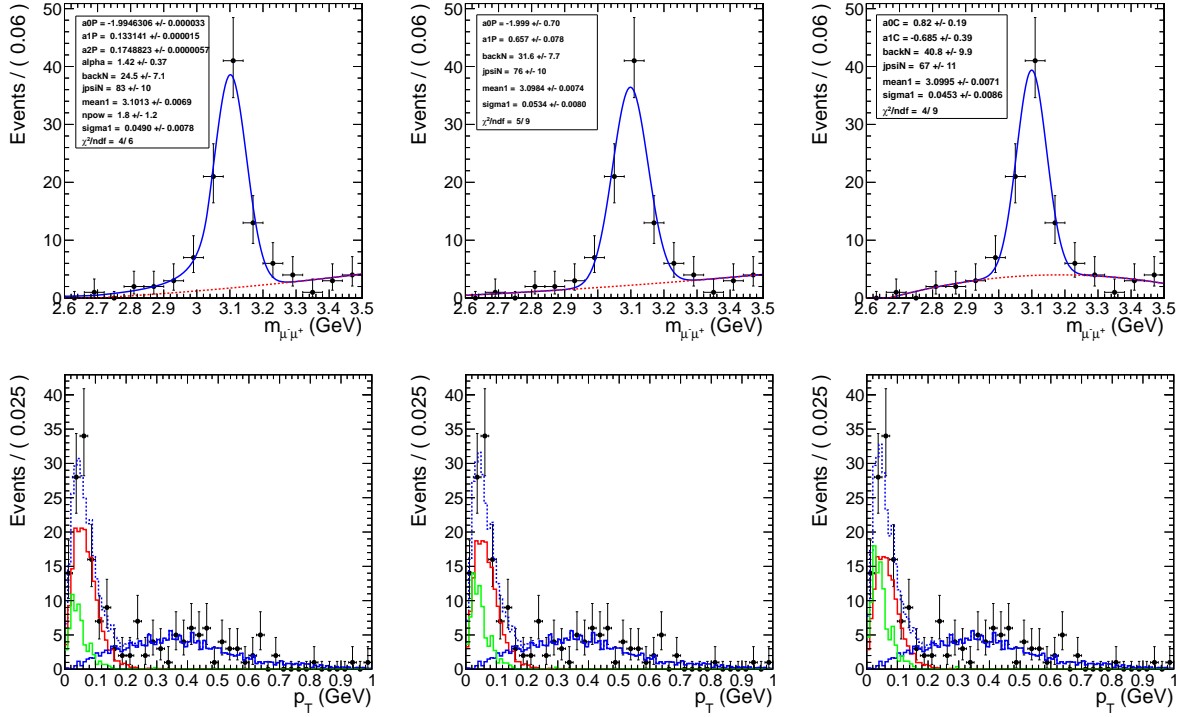


Figure 1.20: Various mass distribution fits and the corresponding  $p_T$  template fit.

fits the background to a 2nd order Cheby-Chev polynomial. Because the Cheby-Chev peaks just below the  $J/\psi$  peak, this fit overestimates the background and in turn underestimates the signal contribution. The Gaussian fit with a linear background however does a reasonable job of fitting both the background and the signal.

From these three fits an upper and lower bound of the systematics due the choice of fit functions was estimated. The difference between the Gaussian-Linear fit and the Crystal Ball-polynomial fit was taken as an upper bound. The difference between the Gaussian-Linear fit and the Gaussian-Cheby-Chev fit was taken as a lower bound. The overall systematic uncertainty due to the choose of mass fit functions is found to be +9.5% -12%.

### 1.7.3 Mass fit

Fig. ?? demonstrates the small dependence the raw  $J/\psi$  yield has on the fitting function. Both fit functions agree well, with reduced  $\chi^2$  values below one. The Crystal ball fit give an upper estimate

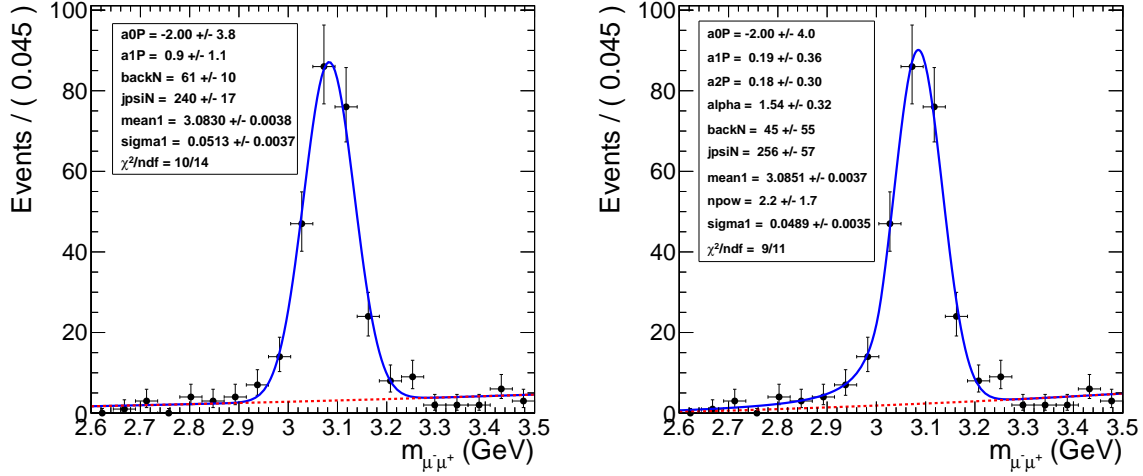


Figure 1.21: Mass fit to  $J/\psi$  using Gaussian (Left) and Crystal Ball (Right) for the signal and a polynomial for the background

for the  $J/\psi$  yield. The Gaussian fit gives an lower estimate. The main difference comes from the lower mass tails. In the Crystal ball fit the lower tail is considered to be signal due to shifting of the mass spectrum to lower mass due to radiation from the final state muons. In the Gaussian fit the lower mass tail is considered to be background and the signal is sharper.

As check on the simultaneous  $p_T$  and mass fit, the mass fit is done using mass templates from STARlight.

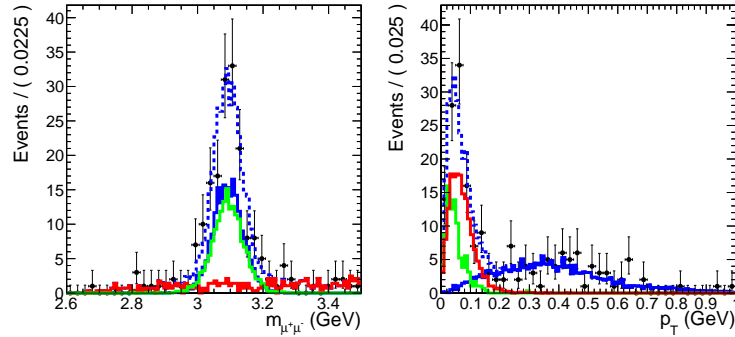


Figure 1.22: Simultaneous fit to the mass and  $p_T$  using mass templates for the mass fit.



#### 1.7.4 MC acceptance

The MC derived acceptance correction factors depend on the input physics generator. The underlying  $p_T$  distribution was assumed to be correctly described by STARlight for the coherent cross section measurement. To estimate the effect of changing the underlying  $p_T$  distribution on the acceptance measured from the MC, the incoherent sample was used to correct the coherent yield. By using the broader  $p_T$  distribution of the incoherent process, an estimate of acceptance measurements dependence on the assumed shape of the  $p_T$  distribution was obtained. The systematic uncertainty due to the dependence of the acceptance correction on the  $p_T$  distribution of the input physics generator was estimated by the difference between the correction factors from the coherent and incoherent MC samples. Half the difference was used as the estimate and was found to be 1.1%.

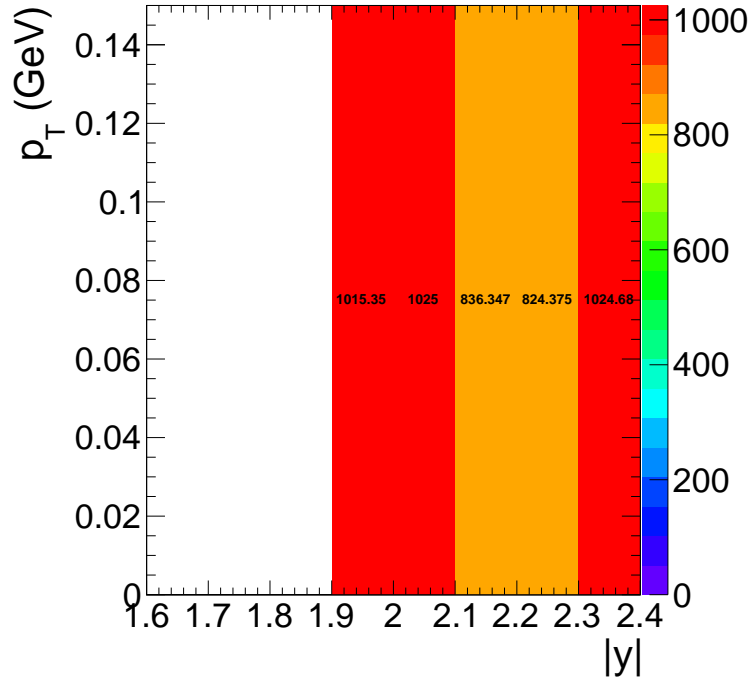


Figure 1.23: Yields corrected by the MC incoherent acceptance map.

The effect of polarization was estimated by correcting by the acceptance for an unpolarized  $J/\psi$  sample.

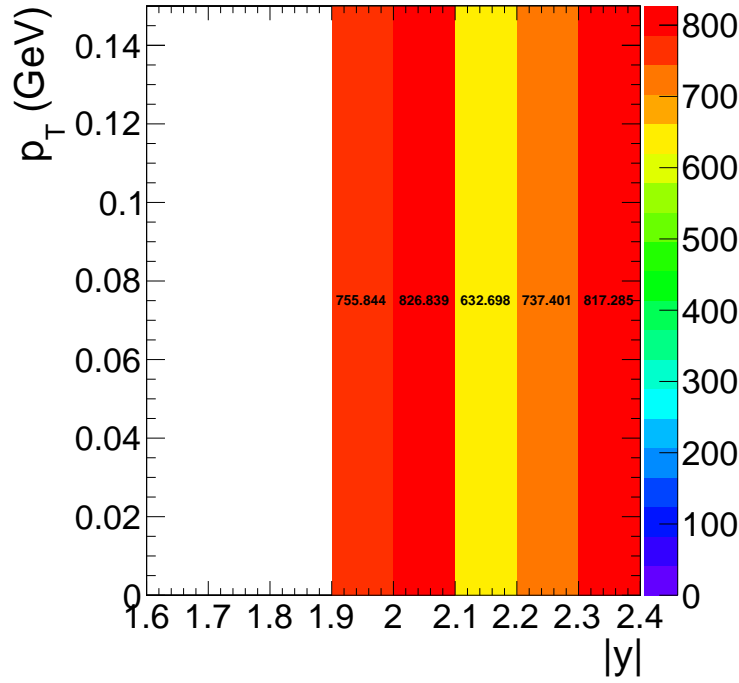


Figure 1.24: Yields corrected by an unpolarized  $J/\psi$  sample.

### 1.7.5 ZDC reconstruction

An additional method for estimating the ZDC neutron thresholds was used to estimate the systematic errors on the threshold measurements. This additional method, used in previous ZDC measurements, differs in the way the signal time slices are used to calculate the signal from each channel. In the standard method, the signal is taken from the sum of time slices 4, 5, and 6. To estimate the event by event noise pedestal the sum of time slice 1 and 2 are used. The signal for an individual ZDC channel is then calculated as the sum of the signal time slices minus the sum of the noise time slices weighted by a factor of 3/2 to account for the differing number of noise versus signal time slices. The advantage of the standard method is that by using multiple signal and noise time slices the signal and noise are effectively averaged reducing time slice to time slice fluctuations. However, by using time slices 1 and 2 for measuring the noise, the noise can only be measured half the time due to unmeasurable negative fluctuations of the dominant low frequency component of the noise.

As in the new method described in Section 1.4, the standard method combines the channels to

create a signal measurement from the whole of each side of the ZDC, one measurement for  $ZDC^+$ , and one for  $ZDC^-$ . The noise subtracted signal from each of the HAD channels are added together. Then the EM section channels are summed. The EM section is weighted by a factor of 0.1 as in the new method. After the weighting the EM and HAD channels are added to each to create one measurement for  $ZDC^+$  and another measurement for  $ZDC^-$ .

Fig. ?? shows the spectra for  $ZDC^+$  and  $ZDC^-$  using the standard method. The same fit used for the new method is applied to standard method. As in the new method, the single neutron threshold is set to  $2\sigma$  below the mean from the fit to the one neutron peak. The multi-neutron threshold was set to  $2\sigma$  above the one neutron peak.

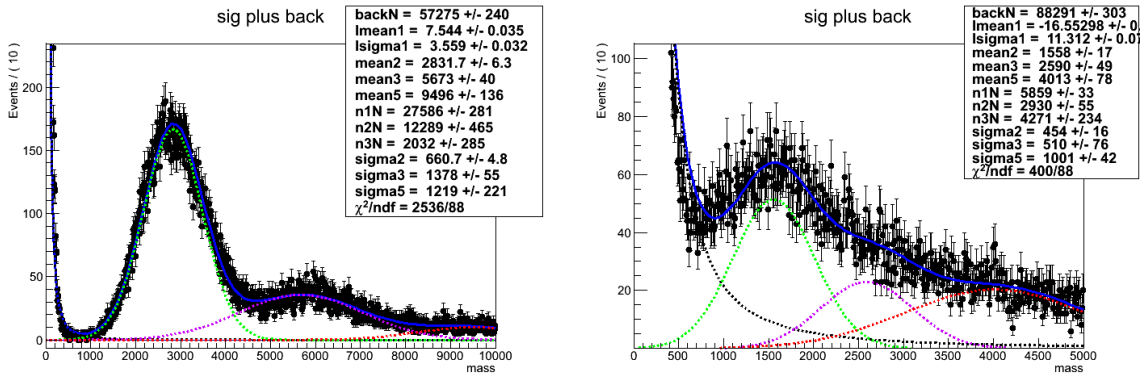


Figure 1.25: Fit to charge spectrum from  $ZDC^-$  (left) and  $ZDC^+$  (right) using the standard reconstruction method

The systematic uncertainty due to the ZDC reconstruction method are estimated from the difference between the UPC  $J/\psi$  candidate yields. Both the reconstruction method and thresholds were changed to calculate the effect of the reconstruction method. The yields for the new and standard ZDC reconstruction method in the  $Xn0n$  break up ~~where~~were found to be 298 and 315 respectively. Half the difference between the two methods was used as an estimated of the systematic uncertainty. The systematic uncertainty due to the ZDC reconstruction method was found to be 2.9%.

## 1.7.6 ZDC reconstruction method comparison

The new method relative to the standard method separates low signal from the noise more effectively for both sides of the ZDC. This is particularly important for  $ZDC^+$  where the 1st HAD section had a lower gain than the other sections. The  $ZDC^+$  and  $ZDC^-$  signals near the one neutron peak using the standard and new reconstruction methods were plotted for comparison in Fig. ??.

In Fig. ??, the shrinking of width of the noise peak around zero in the new method versus the old

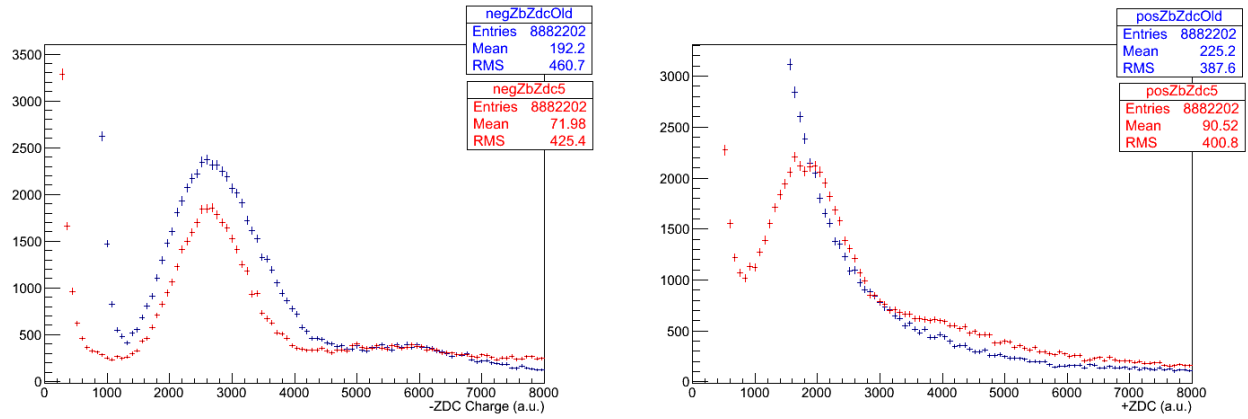


Figure 1.26: Comparison of the **new** ZDC reconstruction method and the **standard** method for  $ZDC^-$  (left) and  $ZDC^+$  (right).

method is apparent for both  $ZDC^+$  and  $ZDC^-$ . For the standard method no single neutron peak is resolved in  $ZDC^+$ , whereas the single neutron peak is resolved using the new method.

Timing cuts were applied to enhance the signal relative to the background in order to resolve the one neutron peak in  $ZDC^+$  using the standard method. Because the products of the collision are synced with time slice 4, noise can be rejected by selecting channels where the maximum signal falls into time slice 4. The noise will have no preferred time slice (see Fig. 1.4). Using this fact, signal can be preferably selected by requiring that the hadronic channels of the ZDC have a peak signal in the fourth time slice. Through these timing cuts the single neutron peak was recovered using the standard reconstruction for  $ZDC^+$ .

To examine the effectiveness of the timing cuts, event by event noise subtraction was removed from the standard reconstruction. The signal from each channel was taken from time slices 4,5, and 6 with out subtracting 1 and 2. The signal spectrum from  $ZDC^-$  was then plotted with the result

shown in Fig. ?? . As each additional hadronic channel is required to have a maximum signal in

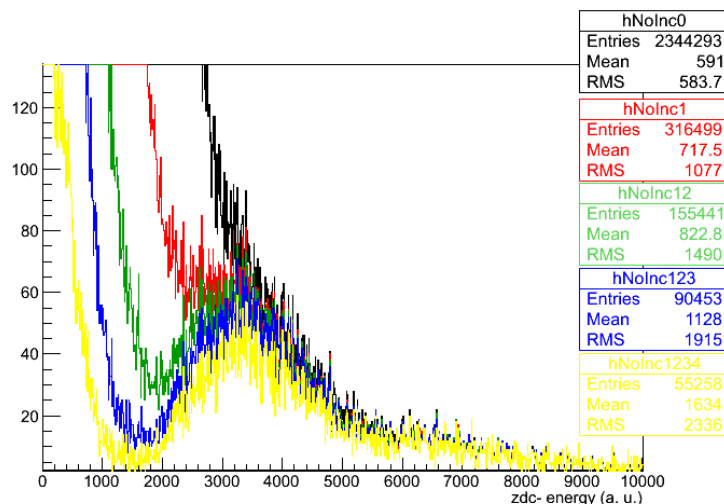


Figure 1.27: Effects of requiring in-time signal in successively more ZDC hadronic channels, no timing, at least **one**, at least **two**, at least **three**, and all **four** HAD channels have a maximum signal in the fourth time slice.

the fourth time slice, the single neutron peak emerges. Fig. ?? demonstrates that the single neutron peak can be recovered from the noise using timing cuts alone.

Using the standard noise subtraction method, the same signal that emerges from the timing cuts alone appear without timing cuts. Fig. ?? confirms that both noise subtraction and the timing

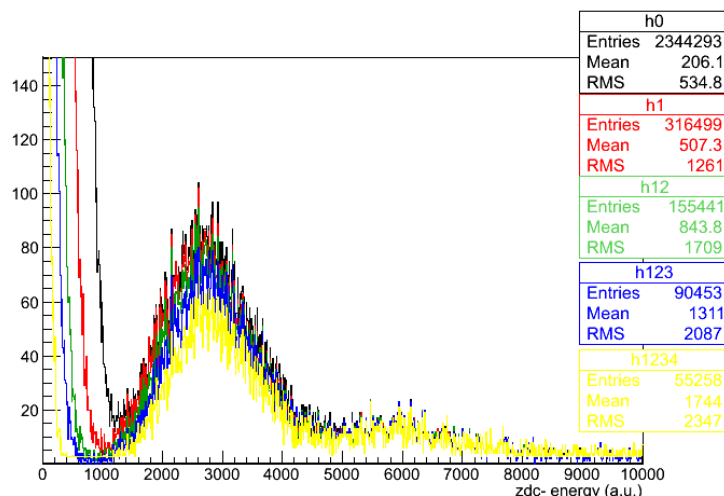


Figure 1.28: Effect of ZDC signal timing requirements after noise subtraction.

requirement produce the same signal. This gives confidence that the signal is not an artifact of

either cut, but the true neutron signal.

Fig. ?? and Fig. ?? demonstrate the consistence of the using timing cuts and noise subtraction to enhance the signal neutron peak. Fig. ?? confirms the legitimacy of the timing requirement method in  $ZDC^-$  by showing the that the same signal emerges from the noise subtraction method as the timing method. Fig. ?? demonstrates the corresponds between the new noise subtraction method and the standard method on in  $ZDC^-$  where signal is better separated from the electronic noise. This allows for confidence that the signal seen in  $ZDC^+$  using the new method is the one neutron peak.

### 1.7.7 ZDC trigger efficiency

The ZDC trigger efficiency measurement is sensitive to the underlying neutron distribution. The more neutrons that high the ZDC the higher the trigger efficiency will be. To estimate the effect the input sample has on the efficiency, the ZDC trigger efficiency was measured from five different samples. The Table ?? shows the results from the five samples. Both the new and standard ZDC reconstruction methods are shown for comparison.

The amount of electronic noise in the sample also effects the measurement. The more noise sits below the one neutron peak, the worse the efficiency is. In Table ??, the Zero Bias sample compared the Zero Bias sample with the timing cuts the described in the previous section shows a significant increase in efficiency in the sample with reduced noise. The same increase is seen when comparing the ZDC triggered sample with the ZDC triggered sample that also requires a pixel track. The effect of the electronic noise is also present in the difference seen in using the two methods. As seen in Fig. ??, the new reconstruction method shows better separation of the one neutron peak from the electronic noise, in particular in  $ZDC^+$  where the signal gain is lower. For this reason, the Zero Bias data, which contains that largest contribution from electronic noise, shows the most separation between the two methods and give the lowest estimate for the ZDC trigger efficiency.

The systematic uncertainty due to the uncertainty in the underlying distribution was estimated

ZDC Side	Reco Method	$N_{events}$	$N_{trig}$	$\epsilon_{ZDC}$
(ZDC <sup>+</sup> or ZDC <sup>-</sup> ) and 1 pixel track				
ZDC <sup>-</sup>	1	72946	71688	$0.982 \pm 0.005$
ZDC <sup>-</sup>	2	73028	71706	$0.9819 \pm 0.005$
ZDC <sup>+</sup>	1	76137	71786	$0.9429 \pm 0.005$
ZDC <sup>+</sup>	2	76132	71859	$0.9439 \pm 0.005$
(ZDC <sup>-</sup> or ZDC <sup>+</sup> ), 1 pixel track, and L1 EG trigger				
ZDC <sup>-</sup>	1	613758	602123	$0.9810 \pm 0.0018$
ZDC <sup>-</sup>	2	614014	601863	$0.9802 \pm 0.0018$
ZDC <sup>+</sup>	1	643905	602671	$0.9360 \pm 0.0017$
ZDC <sup>+</sup>	2	647888	603089	$0.9309 \pm 0.0017$
(ZDC <sup>-</sup> or ZDC <sup>+</sup> ), 1 pixel track, and L1 Muon trigger				
ZDC <sup>-</sup>	1	65466	63376	$0.9681 \pm 0.0054$
ZDC <sup>-</sup>	2	65543	63358	$0.9667 \pm 0.0054$
ZDC <sup>+</sup>	1	71929	63512	$0.8830 \pm 0.0048$
ZDC <sup>+</sup>	2	72932	63582	$0.8718 \pm 0.0047$
Zero Bias with ZDC timing cuts				
ZDC <sup>-</sup>	1	88676	84429	$0.9521 \pm 0.0046$
ZDC <sup>-</sup>	2	88480	84202	$0.9517 \pm 0.0046$
ZDC <sup>+</sup>	1	59878	54728	$0.9140 \pm 0.0054$
ZDC <sup>+</sup>	2	60467	54733	$0.9052 \pm 0.0053$
(ZDC <sup>-</sup> or ZDC <sup>+</sup> )				
ZDC <sup>-</sup>	1	30986	30333	$0.9789 \pm 0.0079$
ZDC <sup>-</sup>	2	31029	30339	$0.9778 \pm 0.0079$
ZDC <sup>+</sup>	1	39178	30164	$0.7699 \pm 0.0059$
ZDC <sup>+</sup>	2	35703	30443	$0.8527 \pm 0.0067$
Zero Bias				
ZDC <sup>-</sup>	1	109967	101598	$0.9239 \pm 0.0040$
ZDC <sup>-</sup>	2	110230	101561	$0.9214 \pm 0.0040$
ZDC <sup>+</sup>	1	253241	86660	$0.3422 \pm 0.0013$
ZDC <sup>+</sup>	2	156336	87401	$0.5591 \pm 0.0024$

Table 1.11: ZDC trigger efficiencies for ZDC reconstruction method 1 and 2 for different trigger samples

by calculating the standard deviation of the least extreme values from Table ???. Any value greater than three standard deviations from the mean was thrown out.

### 1.7.8 Tag and probe

The main purpose for fitting the mass spectra to estimate the efficiency is to separate the background from true signal. The background may not have the same efficiency as the signal, so separating the two is important if this is the case. In the tag and probe fit the signal peak from the  $J/\psi$  resonance is fit to the probes, passing probes, and failing probes alike (see Fig. 1.15). The signal shape, if from the same physical signal, will be identical in each of the three distributions. The background for the passing and failing probes is fit using different parameters for the background because the background may come from different physical processes than the signal or non-physical sources like combinatorial backgrounds or misidentified fake particles. When the background comes from sources other than the physical signal, the background may give an efficiency estimate that is lower than the signal.

The trigger efficiency measured by the tag and probe method depend on the fitting functions use to estimate the background and signal contributions. Depending on what functions is used to fit the spectra, the amount of amount of background can be over or underestimated and effect the efficiency measurement. To estimate this effect, the tag and probe efficiencies were additionally measured by counting probes in the  $J/\psi$  mass window. The whole mass window is used to estimate the efficiency including all the events from the mass side bands. In this way, a worst case scenario estimate is given where all background events are included as signal.

From Fig. ??? it is apparent that the choice of fit function and therefore the amount of background from the mass side bands is included in the signal measurement has very little effect on the tag and probe efficiency measurement. The small effect of including the side bands is due to the side bands being comprised mostly of photon-photon events. Because this background is neither decays from other particles like pions nor is it non-physical background like combinatorics, the efficiency for muons from the sidebands are nearly identical to  $J/\psi$  signal. The photon-photon



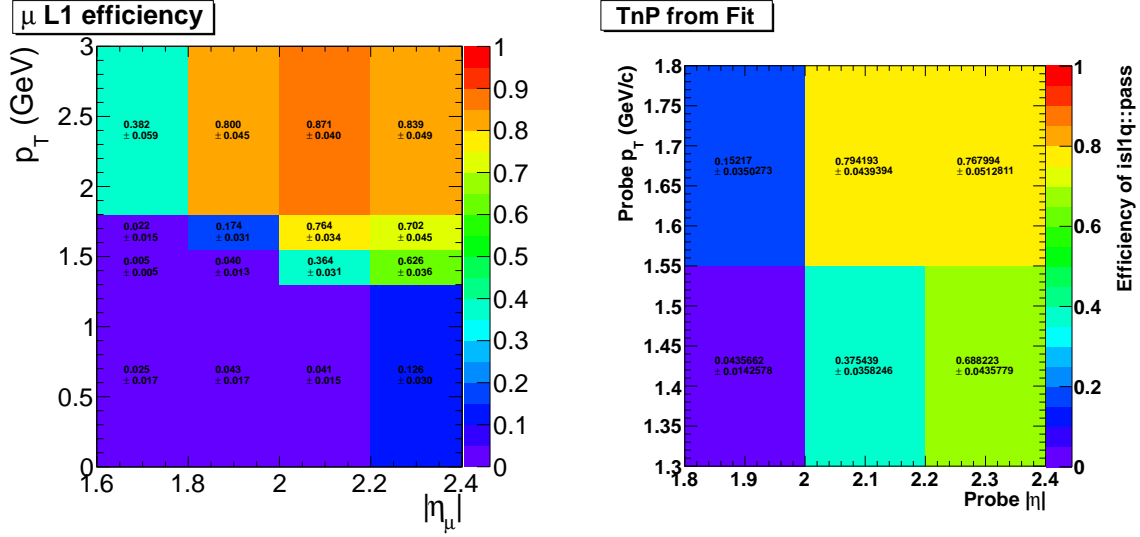


Figure 1.29: Tag and probe trigger efficiencies from counting (left) compared to fitting (right)

process directly produces two muons just like the  $J/\psi$ , therefore efficiency estimated from the side bands has little effect on the measurement because of this similarity. The counting and fitting trigger efficiency measurements agree within statistical uncertainties, so this uncertainty was taken to be negligible.

## 1.7.9 MC vs Data compairson

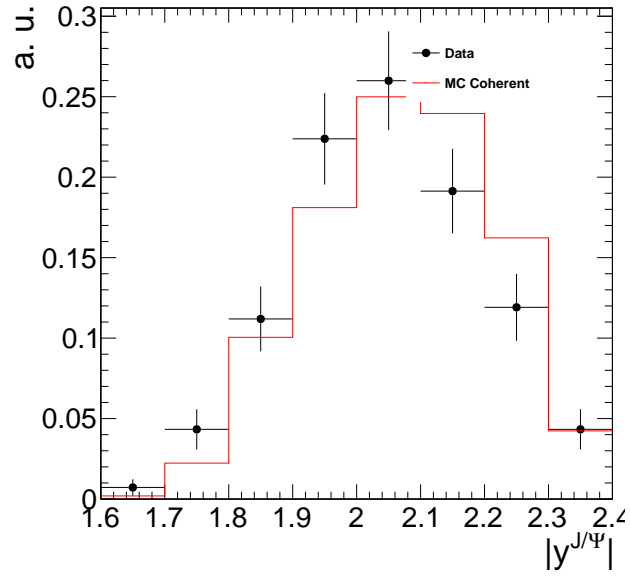


Figure 1.30: Comparison of the of the dimuon rapidity distributions between coherent MC sample and Data.

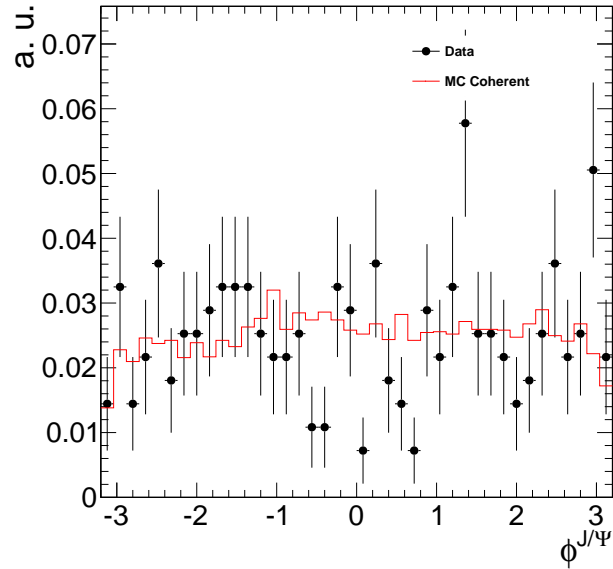


Figure 1.31: Comparison of the of the dimuon  $\phi$  distributions between coherent MC sample and Data.

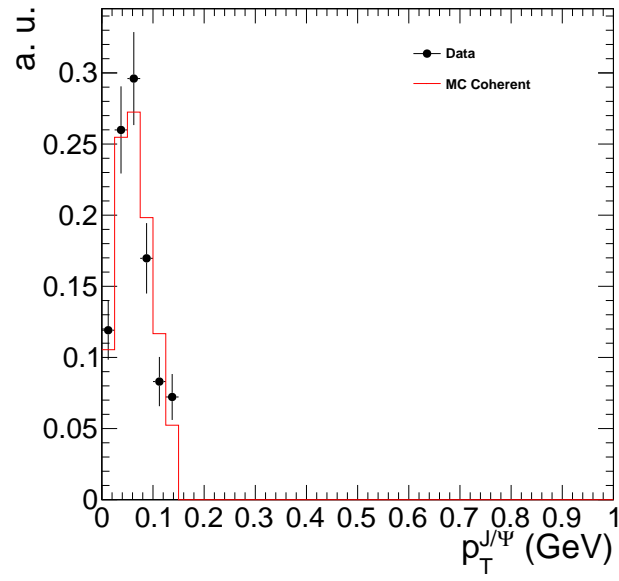


Figure 1.32: Comparison of the of the dimuon  $p_T$  distributions between coherent MC sample and Data.

# Chapter 2

## Results

### 2.1 Coherent cross section

~~For the coherent~~ The main results of this thesis are give here: the cross section for coherent  $J/\psi$  production, the incoherent  $J/\psi$  cross section, the cross section for muon pairs from photon-photon interactions, the ratio between break up mode yields, and the rapidity correlations between dimuon candidates and neutrons in the ZDC.

### 2.1 Coherent cross section

The coherent cross section in calculated from the following equation:

$$\frac{d\sigma_{co}^{J/\psi}}{dy} =$$

$\Delta y \mathcal{L}_{int} \epsilon_{ZDC} \epsilon_{p_T} BR_{\mu^+\mu^-}$  (2.1) where  $N_{cor}$  is corrected dimuon yield,  $f_{co}$  is the fraction of events that come from the coherent process,  $BR_{\mu^+\mu^-}$  is the branching ratio for  $J/\psi$  to  $\mu^+\mu^-$ ,  $\epsilon_{ZDC}$  is the efficiency for triggering the ZDC,  $\epsilon_{p_T}$  is the efficiency for the 0.15 GeV cut in  $p_T$ ,  $\mathcal{L}_{int}$  is the integrated luminosity, and  $\Delta y$  is the width the rapidity interval.

The raw yield of dimuon candidates was measured after applying the cuts described in Sec-

tion 1.3.

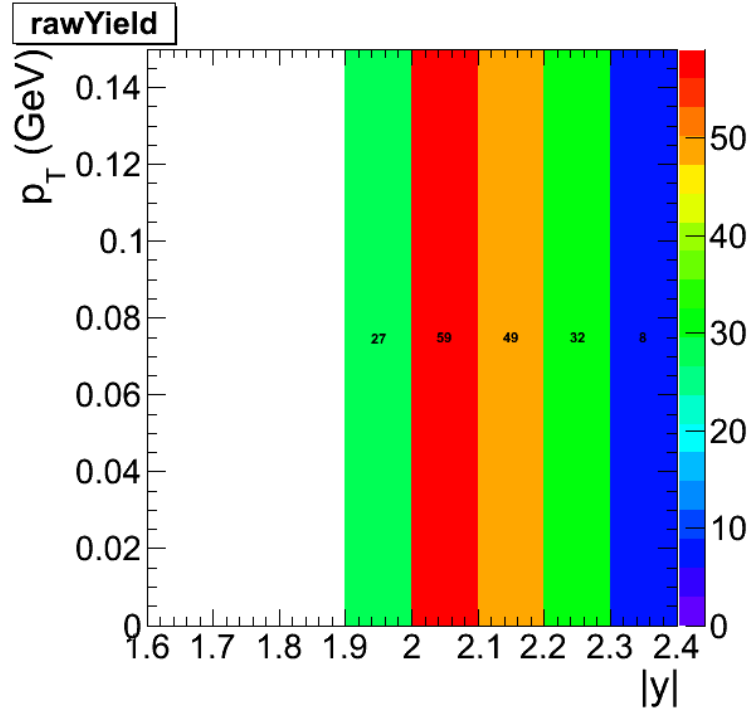


Figure 2.1: Raw yield for the Coherent cross section measurement.

The raw yields were divided by the total efficiency times acceptance factors to produce corrected yields.  $N_{cor}$  was calculated by dividing the raw yields from Fig. ?? by the acceptance and efficiency factor from Fig. 1.18, which combines  $A$  and  $\epsilon_{trigger}^{dimuon}$  as described in Section. 1.6. The corrected yields,  $N_{cor}$ , are shown in Fig. ??.

The corrected yields in the For the coherent cross section measurement,  $N_{cor}$  is taken from the region  $2.0 < |y| < 2.2$  and  $2.1 < |y| < 2.2$  rapidity bins were added together to calculate the cross section. These bins were selected to insure a total acceptance times efficiency greater than 5%.

The contribution from coherent production  $< 2.2$  and  $p_T < 0.15$  GeV to avoid the edges of the detectors acceptance, bin migration in the calculation of  $A$ , and overlap between the coherent and incoherent process. From this procedure the  $N_{cor}$  was measured to be 1903.

To measure  $f_{co}$ , the simultaneous fit shown in Fig. 1.11 was used. The normalizations for each of the three components to the signal are fixed by the fit as described in Section 1.5. The normalized coherent template is integrated up to 0.15 GeV in  $p_T$  and divided by the integral of the

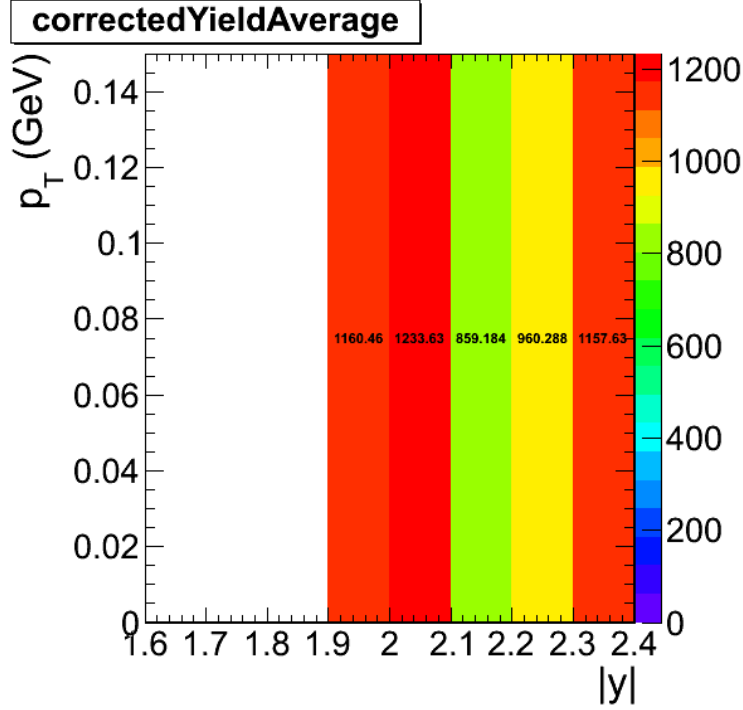


Figure 2.2: Corrected yields for the coherent  $p_T$  region.

data  $p_T$  spectrum up to 0.15 GeV. The statistical error taken from the fit,  $f_{co} = 0.60 \pm 0.11$ .

The two efficiency terms,  $\epsilon_{ZDC}$  and  $\epsilon_{p_T}$ , were measured from data and MC respectively. As described in Section 1.4,  $\epsilon_{ZDC}$  was measured in the from the ZDC triggered data set by dividing the number of events both fire the ZDC trigger and pass the one neutron threshold.  $\epsilon_{ZDC}$  was measured to be 0.96 with a negligible statistical error. The efficiency of the 0.15 GeV  $p_T$  cut was estimated from the template fit in Fig. ???. The first three bins are used to estimate the contribution below 150 MeV MC by dividing the number of events that are lost by applying the  $p_T$  cut after all other cuts are applied. From this method  $\epsilon_{p_T} = 0.95$ .

The remaining two terms,  $\mathcal{L}_{int}$  and  $BR_{\mu^+\mu^-}$ , depend on Ref. [?] and Ref. [?]. Ref. [?] describes the method of using activity in HF to measure the luminosity. From this method,  $\mathcal{L}_{int}$  was measured to be  $143.3 \mu b^{-1} \pm 7.2$ .  $BR_{\mu^+\mu^-}$  from Ref. [?] is  $0.0593 \pm 0.0006$ . From Equation ??,  $\frac{d\sigma_{co}^{J/\psi}}{dy} = 368 \text{ mb}$ .

## 2.2 Incoherent cross section

## 2.3 Break up ratios

In Table ?? the ratio between raw yields for different break up modes are shown.

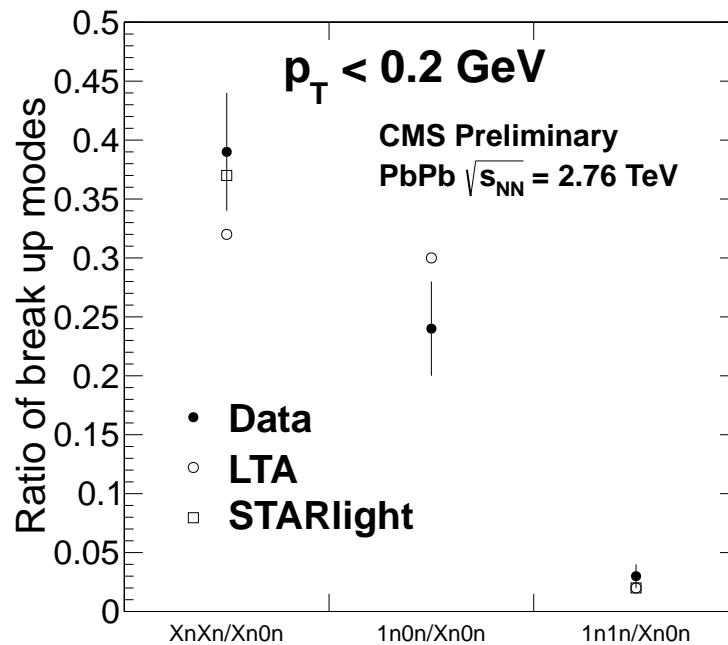


Figure 2.3: Ratio between  $J/\psi$  yeilds  $X_n X_n$  and  $1_n 0_n$  break-up modes compared the  $X_n 0_n$  break-up mode for  $J/\psi$  with  $p_T$  below 150 MeV.

Fig. ?? and Fig. ?? compare the raw break up ratios two STARlight and LTA predictions.

In Table ?? the ratio between break up modes are shown for different theories and processes.

Table 2.1: Number of  $J/\psi$  integrated over  $p_T$  and  $y$  with statistical uncertainty.

	$X_n X_n / X_n 0_n$	$1_n 0_n / X_n 0_n$	$1_n 1_n / X_n 0_n$
STARlight coherent	0.37	-	0.02
Zhalov coherent	0.32	0.30	0.02
STARlight incoherent	0.37	-	$0.007 \pm 0.02$

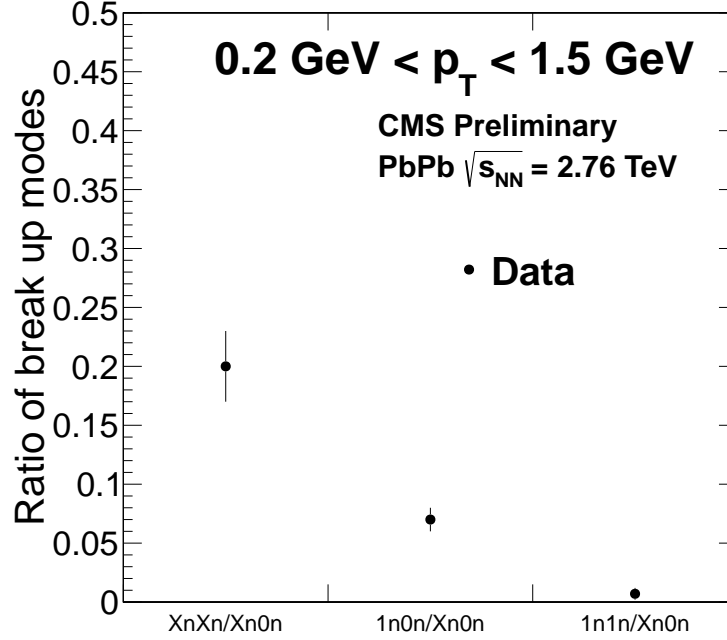


Figure 2.4: Ratio between  $J/\psi$  yeilds  $X_n X_n$  and  $1_n 0_n$  break-up modes compared the  $X_n 0_n$  break-up mode for  $J/\psi$  with  $0.2 < p_T < 1.5$  GeV.

## 2.4 diMuon-neutron correlations

The invariant mass distribution for different break-up modes is show for the coherent and incoherent  $J/\psi$  on the Fig. ?? and Fig. ?? respectively.

The number of the coherent and incoherent  $J/\psi$  for each break-up mode are given in the Tab. ?. The ratios between the modes  $X_n X_n$ ,  $1_n 0_n$ ,  $1_n 1_n$  and the mode  $X_n 0_n$  are given in the table Tab. ?. Some of the ratios can be obtained from STARLIGHT and from the Zhalov and thus are given in Tab. ?.

Table 2.2: Number of coherent  $J/\psi$  integrated over  $p_T$  and  $y$  with statistical uncertainty.

	$X_n 0_n$	$X_n X_n$	$1_n 0_n$	$1_n 1_n$
coherent $J/\psi$	$242 \pm 16$	$94 \pm 10$	$58 \pm 8$	$8 \pm 3$
incoherent $J/\psi$	$291 \pm 17$	$57 \pm 8$	$19 \pm 4$	$2 \pm 1$

For statistical reason, further studies concentrate only on the break-up mode  $X_n 0_n$ .

Figure ?? shows the transverse momentum distribution of the  $J/\psi$  (coherent and incoherent) in the



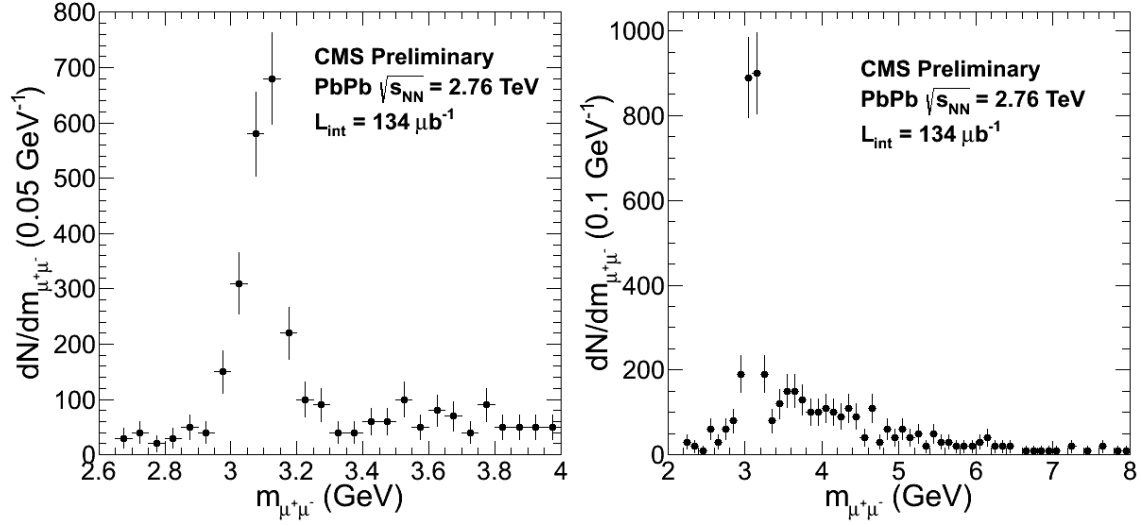


Figure 2.5: Invariant mass spectrum of the opposite signs di-muons originating from the coherent  $J/\psi$  for  $X_n0_n$  breakup mode for two invariant mass regions.

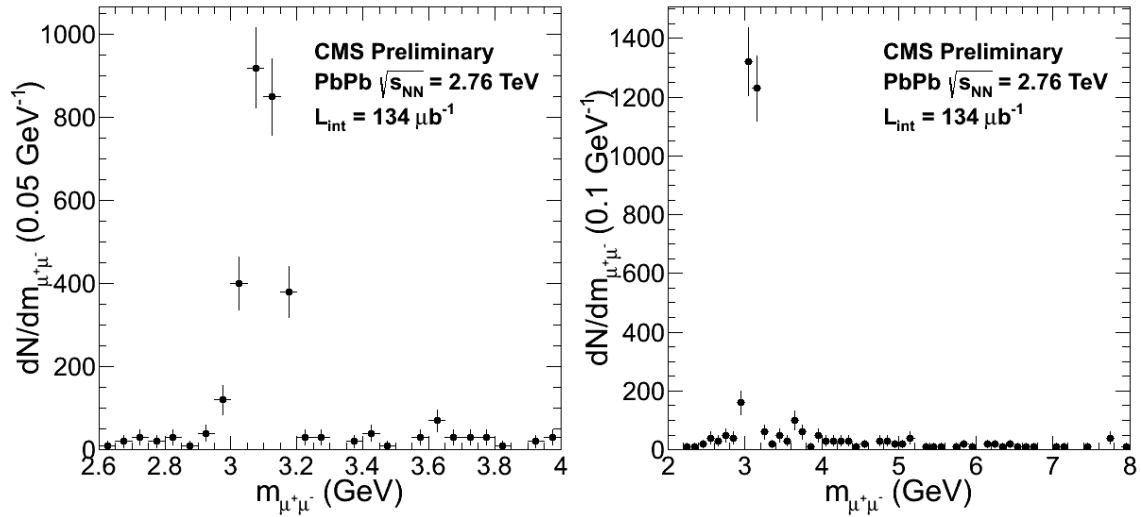


Figure 2.6: Invariant mass spectrum of the opposite signs di-muons originating from the incoherent  $J/\psi$  for  $X_n0_n$  breakup mode for two invariant mass regions.

case when  $J/\psi$  and neutron have the same or opposite rapidity direction. The ratio between the  $J/\psi$  and neutron that have the opposite direction and the  $J/\psi$  and neutron that have the same direction is shown on Fig. ???. The red curve gives the pure theory calculations, the black one gives the theory results that are injected to the detector simulation and thus taking into account experimental bias.

The rapidity distributions of the coherent and incoherent  $J/\psi$  are shown in the Fig. ???. They

Table 2.3: Number of coherent  $J/\psi$  integrated over  $p_T$  and  $y$  with statistical uncertainty.

	$X_n X_n / X_n 0_n$	$1_n 0_n / X_n 0_n$	$1_n 1_n / X_n 0_n$
coherent $J/\psi$	$0.39 \pm 0.05$	$0.24 \pm 0.04$	$0.03 \pm 0.01$
incoherent $J/\psi$	$0.20 \pm 0.03$	$0.07 \pm 0.02$	$0.007 \pm 0.005$

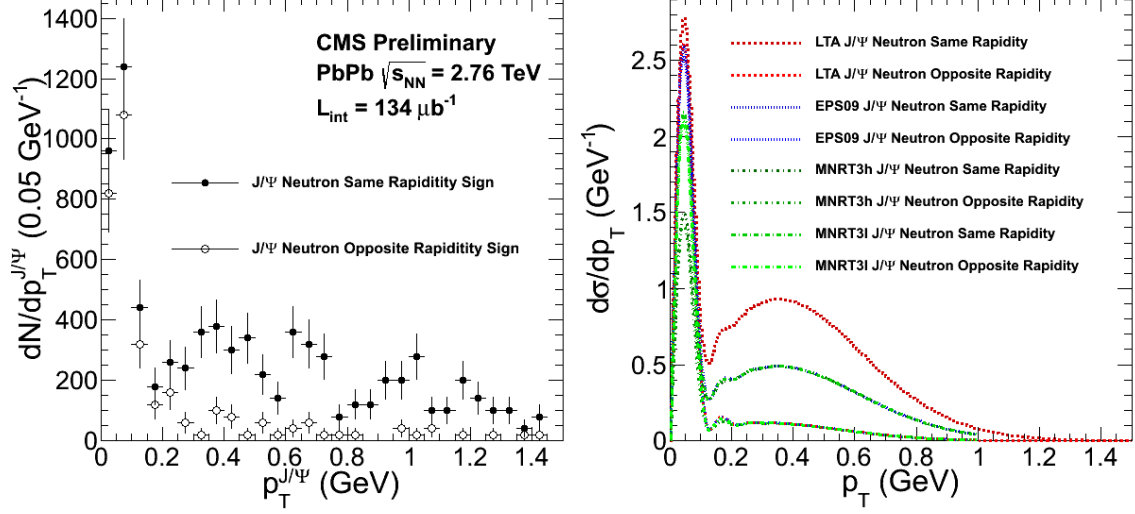


Figure 2.7: Transverse momentum distribution of the  $J/\psi$  when  $J/\psi$  and neutron have the same or opposite rapidity direction from data (left) and from theory (right).

are shown separately for the events firing the  $ZDC^+$  and  $ZDC^-$ . The same distributions are also obtained for the MC and shown in Fig. ???. For the MC the particle gun generator with the input  $p_T$  spectrum from Zhalov's calculation (LTA). The rapidity symmetry for coherent  $J/\psi$  and asymmetry for incoherent  $J/\psi$  are observed in data and MC. These are quantified in the Tab. ??.

Table ?? gives the number of coherent and incoherent  $J/\psi$  separately for the events that fired the  $ZDC^-$  and  $ZDC^+$ . We quote separately the  $J/\psi$  that have the same or opposite rapidity direction to the neutron direction. The ratios, as described below are also given in the Tab. ??:  $R_{ZDC^-}^{y^+/y^-}$  : ratio between the number of  $J/\psi$  having  $y > 0$  to the number of  $J/\psi$  having  $y < 0$  from the events that fired  $ZDC^-$

$R_{ZDC^+}^{y^-/y^+}$  : ratio between the number of  $J/\psi$  having  $y < 0$  to the number of  $J/\psi$  having  $y > 0$  from the events that fired  $ZDC^+$

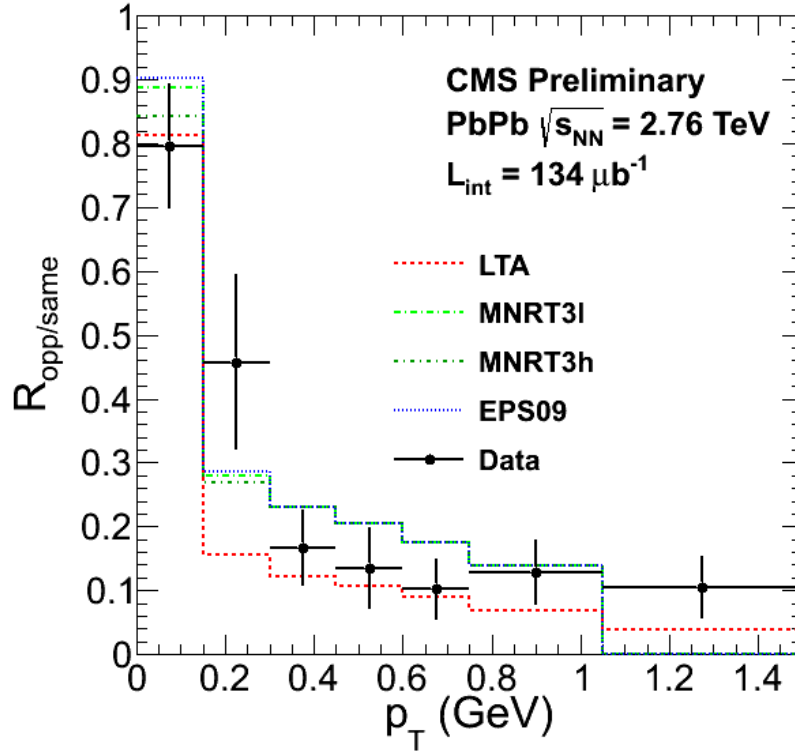


Figure 2.8: Ratio between the transverse momentum distribution of the  $J/\psi$  when  $J/\psi$  and neutron have the opposite direction and the transverse momentum distribution of the  $J/\psi$  when  $J/\psi$  and neutron have the same direction.

The combined ratio  $R_{opp/same}^c$  is calculated as

$$R_{opp/same}^c = \frac{ZDC^- \text{ and } y > 0 + ZDC^+ \text{ and } y < 0}{ZDC^- \text{ and } y < 0 + ZDC^+ \text{ and } y > 0}$$

•  $R_{opp/same}^c$  for coherent  $J/\psi = 0.83 \pm 0.12$ .

•  $R_{opp/same}^c$  for incoherent  $J/\psi = 0.155 \pm 0.021$ .

The correction factors (efficiency, reconstruction) are as following:

•  $\epsilon_{ZDC^-}$ : efficiency of the  $ZDC^-$  of 0.98

Table 2.4: Final number of  $J/\psi$  (for both ZDCs and for two negative and positive rapidity) and ratios with statistical uncertainty.

	ZDC <sup>-</sup> $y < 0$	ZDC <sup>-</sup> $y > 0$	$R_{ZDC^-}^{y^+/y^-}$	ZDC <sup>+</sup> $y < 0$	ZDC <sup>+</sup> $y > 0$	$R_{ZDC^+}^{y^-/y^+}$
coherent $J/\psi$	63	68	$1.08 \pm 0.19$	42	69	$0.61 \pm 0.12$
incoherent $J/\psi$	141	26	$0.184 \pm 0.039$	13	111	$0.117 \pm 0.034$

•  $\epsilon_{ZDC^+}$ : efficiency of the ZDC<sup>+</sup> of 0.94

•  $\epsilon_{\mu^-}$ : efficiency  $\times$  reconstruction of the muons with rapidly  $< 0$ : 1.0

•  $\epsilon_{\mu^+}$ : efficiency  $\times$  reconstruction of the muons with rapidly  $> 0$ : 1.014.

The combined ratio  $R_{opp/same}^{eff}$  corrected with the factors above is calculated as

$$R_{opp/same}^{eff} = \frac{\epsilon_{ZDC^-} \epsilon_{\mu^+} ZDC^- \text{ and } y > 0 + \epsilon_{ZDC^+} \epsilon_{\mu^-} ZDC^+ \text{ and } y < 0}{\epsilon_{ZDC^-} \epsilon_{\mu^-} ZDC^- \text{ and } y < 0 + \epsilon_{ZDC^+} \epsilon_{\mu^+} ZDC^+ \text{ and } y > 0}$$

$R_{opp/same}^{eff}$  is  $0.83 \pm 0.12$ .

•  $R_{opp/same}^{eff}$  for coherent  $J/\psi = 0.83 \pm 0.12$ .

•  $R_{opp/same}^{eff}$  for incoherent  $J/\psi = 0.154 \pm 0.021$ .

If considering 3 significant figures for the representation of the result these values are:

•  $R_{opp/same}^c$  for coherent  $J/\psi = 0.833 \pm 0.124$

•  $R_{opp/same}^c$  for incoherent  $J/\psi = 0.155 \pm 0.021$

•  $R_{opp/same}^{eff}$  for coherent  $J/\psi = 0.828 \pm 0.124$

•  $R_{opp/same}^{eff}$  for incoherent  $J/\psi = 0.154 \pm 0.021$

This shows that in this measurement the efficiencies factors are negligible.

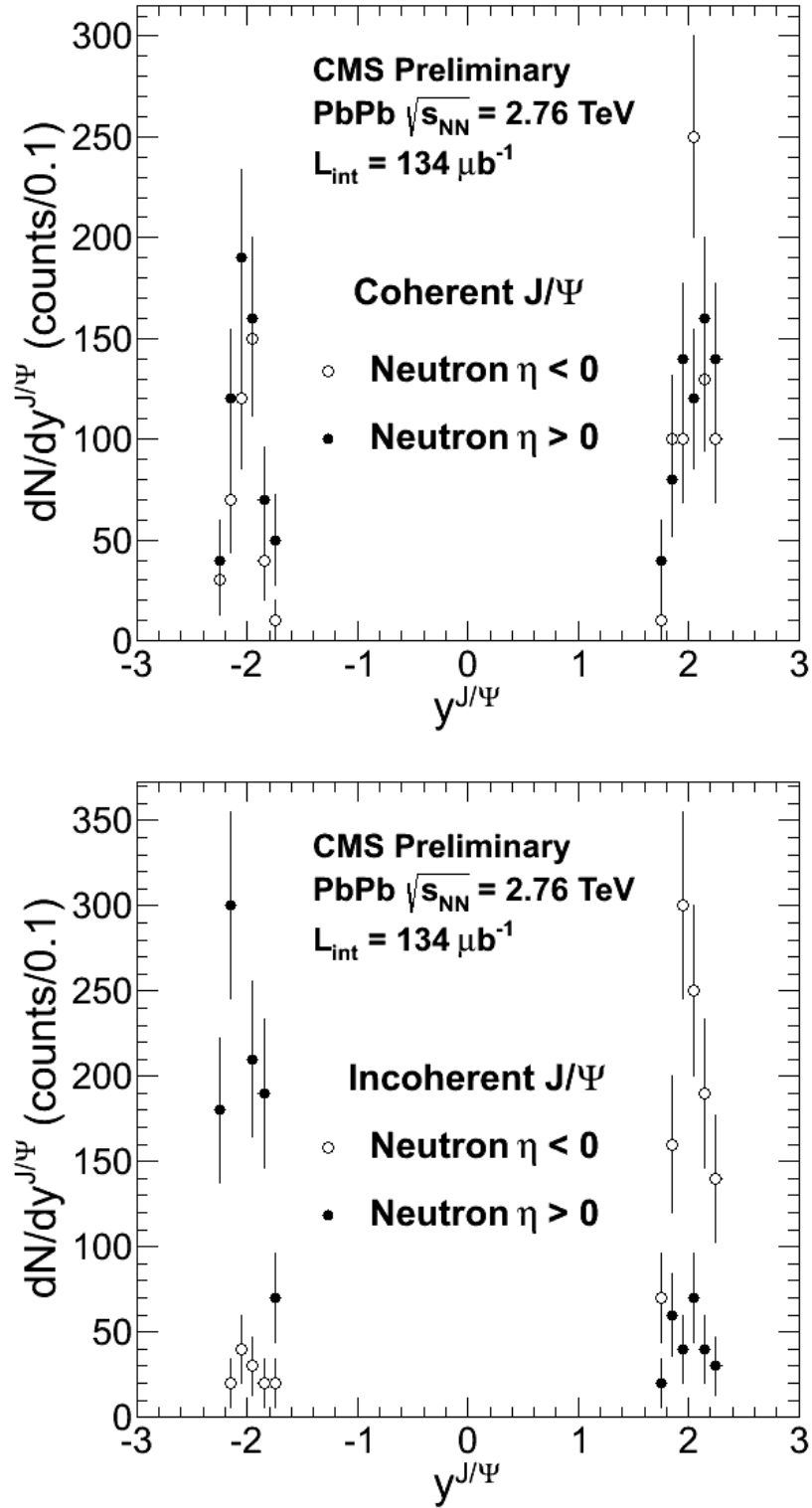


Figure 2.9: The rapidity distribution of the coherent (top) and incoherent (bottom)  $J/\psi$  for the  $ZDC^+$  and  $ZDC^-$ .

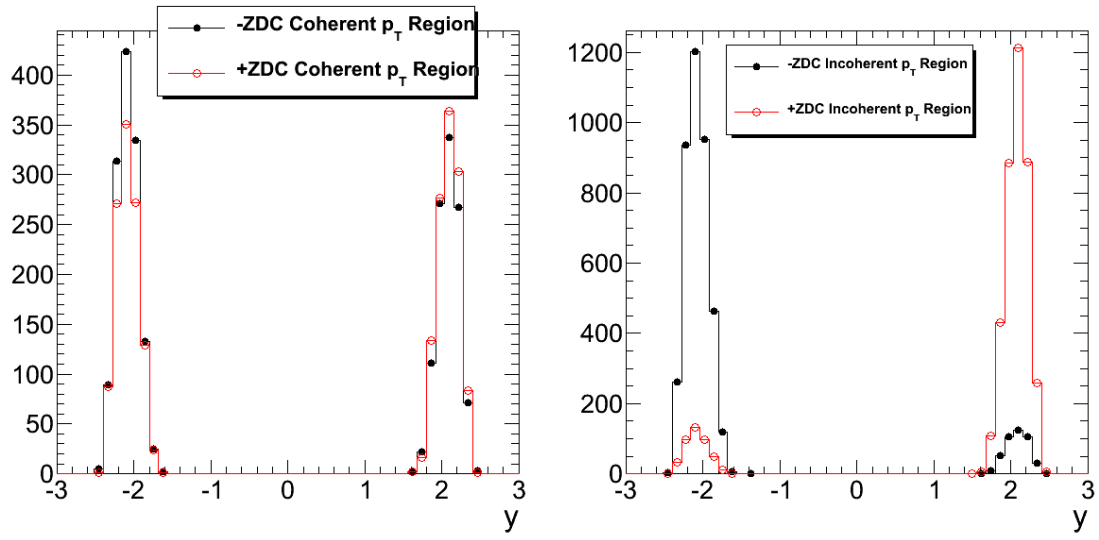


Figure 2.10: The rapidity distribution of the coherent (left) and incoherent (right)  $J/\psi$  for the  $ZDC^+$  and  $ZDC^-$  from MC (particle gun with customized  $J/\psi p_T$  input distribution).